ELSEVIER

Contents lists available at ScienceDirect

# Ceramics International

journal homepage: www.elsevier.com/locate/ceramint





# Microstructural characterization and equibiaxial flexural strength of $\text{CeO}_2$ and $\text{Ti-doped CeO}_2$

Adrianna E. Lupercio <sup>a,b</sup>, Riley C. Van Horn <sup>a,b</sup>, Cayden Doyle <sup>a,b</sup>, Alex Nadermann <sup>c</sup>, Andrew T. Nelson <sup>d</sup>, Brian J. Jaques <sup>a,b,\*</sup>

- <sup>a</sup> Boise State University, Micron School of Materials Science and Engineering, Boise, ID, USA
- b Center for Advanced Energy Studies, Idaho Falls, ID, USA
- <sup>c</sup> Northwest Nazarene University, Nampa, ID, USA
- <sup>d</sup> Oak Ridge National Laboratory, Oak Ridge, TN, USA

#### ARTICLE INFO

Handling Editor: Dr P. Vincenzini

#### ABSTRACT

In this study, the synthesis of  $CeO_2$  and titanium dioxide ( $TiO_2$ ) doped  $CeO_2$  (TDC) monoliths are investigated, and their fracture strength is assessed using an equibiaxial flexure testing technique at room temperature. Pellets were synthesized using conventional powder processing and sintering methods to produce the desired characteristics. The  $TiO_2$  dopant concentration was optimized at 0.1 wt %  $TiO_2$  to obtain dense, solid-solution pellets with an enhanced grain microstructure. A ball-on-ring fixture was used to obtain the TRS and Weibull parameters of over 30 pellets for  $CeO_2$  and 0.1 wt % TDC to compare fracture behavior. The TRS of  $CeO_2$  pellets ranged from 88 to 160 MPa and the TRS of 0.1 wt % TDC pellets ranged from 102 to 171 MPa, both being consistent with published values. Weibull parameters, such as characteristic strength and Weibull modulus, were extracted as 129 MPa and 8.5 for  $CeO_2$  and 150 MPa and 9.3 for 0.1 wt % TDC, respectively. Although Hertzian contact damage was observed on compressive surfaces, failure initiation occurred on the tensile surfaces of both types of samples. Fracture surface analysis for  $CeO_2$  indicated a predominantly intergranular fracture while 0.1 wt % TDC had a predominantly transgranular fracture mode. The TRS of 0.1 wt % TDC resulted in increased Weibull parameters when compared to  $CeO_2$ , indicating sample chemistry and microstructure impact mechanical behavior for these samples.

# 1. Introduction

Cerium, one of the most abundant rare-earth metals, has gained substantial attention in recent years, particularly in its oxide form (cerium dioxide, CeO<sub>2</sub>). Its cubic fluorite structure, thermochemical stability, oxygen mobility and storage, optical, catalytic, electrolyte, and redox capabilities make it a material of extensive utility in modern technology [1]. CeO<sub>2</sub> is widely used in grinding and polishing agents, for optics and microelectronics, components in gas sensors, as a catalyst in automotive and biomedical applications, for wastewater treatment, an electrode material, and serves as a non-radioactive surrogate for UO<sub>2</sub> and PuO<sub>2</sub> nuclear fuels given it's similar thermophysical properties and fluorite crystal structure [2,3]. Moreover, CeO<sub>2</sub> has a promising potential as an electrolyte material in intermediate temperature-solid oxide fuel cells (IT-SOFCs), which have an important role to play in the transition to carbon neutral sources of energy [4]. Historically, SOFCs

have largely used zirconia ( $ZrO_2$ ) based solid electrolytes; however, varying compositions of doped  $CeO_2$  are being investigated to reduce the operational temperature range from the conventional 800–1000 °C to intermediate temperatures spanning 500–700 °C [5].

The traditional ZrO<sub>2</sub> electrolyte requires high operational temperatures to maintain oxygen diffusion efficiency and maintain an electrolyte thickness that can be readily handled. Hence, reducing operating temperatures to an intermediate temperature requires either reduced electrolyte thickness, more innovative electrode materials, or alternate electrolyte materials to maintain the SOFC efficiency [6]. The most feasible path points toward engineering alternate electrolyte materials with high ionic conductivity at intermediate temperatures, which has spurred many studies investigating the doping of CeO<sub>2</sub> with lanthanides (i.e., Gd<sup>3+</sup>, and Sm<sup>3+</sup>) [7]. However, despite the excellent ionic conductivity of Sm doped CeO<sub>2</sub> (SDC) and Gd doped CeO<sub>2</sub> (GDC) electrolytes, they have a poor sintering activity and an increased electrical

<sup>\*</sup> Corresponding author. Boise State University, Micron School of Materials Science and Engineering, Boise, ID, USA. *E-mail address:* brianjaques@boisestate.edu (B.J. Jaques).

conductance at low oxygen partial pressures [8]. Moreover, although the oxygen ion conductivity of pure CeO2, SDC, and GDC is greater than traditional ZrO2 at intermediate temperatures, improving their density at lower sintering temperatures is necessary for IT-SOFC performance and commercial viability. Currently, SDC and GDC electrolytes require an electrolyte thickness that is still very thin ( $\sim$ 10–100  $\mu$ m), resulting in a high failure rate when handling, making them difficult to produce commercially. An alternative fabrication method being investigated for IT-SOFCs is an anode supported electrolyte where the electrolyte material is deposited onto the anode and co-sintered. This alternative method presents additional challenges where sintering temperatures above 1200 °C create an interlayer resistance between the electrolyte and anode, which effectively reduces the oxygen ion conductivity. Therefore, to produce an efficient electrolyte material for intermediate temperatures, the material must be dense, thermally stable, have a high oxygen ion conductivity, and have the capacity to be sintered at lower temperatures for anode supported electrolytes [9]. Additionally, the grain boundary resistance, resulting from the inferior ion conductivity of the grain boundaries, is attributed to the space-charge effect at low and intermediate temperatures. This effect leads to a decreased concentration of oxygen vacancies in the grain surface and a decreased ionic conductivity [10-12]. Alternatively, larger grains can enhance microstructural stability during operation whereas fine-grained electrolytes experience grain growth during high-temperature operation, causing changes in performance over time. Therefore, it is desirable to produce electrolytes with larger grains and reduced grain boundary area to improve ionic conductivity and operational stability. It is important to note that larger grains may adversely affect the mechanical properties of the electrolyte.

Dopants that can serve as a sintering aid in  $CeO_2$  are of interest to enhance grain size and reduce the sintering temperature of anode supported electrolytes and prevent the formation of an interface layer during co-sintering. Accordingly, dopant additives with severely undersized cations, such as  $TiO_2$  and MgO, have been identified as sintering aids and grain growth promoters in  $CeO_2$  [13]. Although  $TiO_2$  has been shown to enhance the grain boundary mobility in  $CeO_2$  [13], secondary  $TiO_2$  phases in the  $CeO_2$  matrix could negatively impact the ionic conductivity [8]. Previous studies have shown that doping  $CeO_2$  with less than 0.1 mol %  $TiO_2$  can increase grain growth while maintaining a solid  $(Ce-Ti)O_x$  solution [8].

Along with improving sinterability, microstructure, and maintaining phase stability of CeO<sub>2</sub> based IT-SOFCs, it is important to understand how chemical and microstructural changes impact fracture strength, which influences their mechanical stability. SOFCs are subjected to cyclic mechanical and thermo-mechanical stresses resulting from the CeO<sub>2</sub> redox reaction and thermal gradients due to operating conditions [14, 15]. The broad use and applicability of CeO<sub>2</sub> in modern technology has spurred many studies investigating the chemical, microstructural, thermal, and electrical properties of CeO<sub>2</sub> and doped CeO<sub>2</sub> [16,17]. While mechanical properties, such as the elastic modulus, hardness, and creep, have been investigated for CeO<sub>2</sub> and doped CeO<sub>2</sub>, statistically relevant mechanical fracture behavior, such as transverse rupture strength (TRS) (i.e., flexural strength), is lacking [18].

Obtaining CeO<sub>2</sub> statistical baseline fracture strength data is important when gaining insight into how dopants and sintering aids aimed at enhancing oxygen ion conductivity and sinterability impact fracture behavior. A limited number of studies report on the TRS of CeO<sub>2</sub> and its Weibull parameters, such as characteristic strength and Weibull modulus, are not reported in the literature (Table 3). TRS studies of doped CeO<sub>2</sub> focus on SDC and GDC samples also contain insufficient test samples to determine Weibull parameters. In addition, to the authors' knowledge, TRS studies for TiO<sub>2</sub> doped CeO<sub>2</sub> (TDC) have not been performed and Weibull parameters are not available.

TRS tests of ceramics have been traditionally performed using ASTM standard C1161-13 [19] which requires rods of rectangular bars with tight tolerances. Producing sufficient bend bar test samples for a

statistical analysis (N > 30) can incur significant costs and time demands, primarily because machining test samples is essential for achieving the precise sample geometry needed. The complexity and cost of fabricating bend bars may be prohibitive to performing a comprehensive statistical analysis. In addition, the sample fabrication process introduces extraneous surface flaws which can greatly influence the mechanical properties of ceramic materials [20,21]. Alternatively, biaxial flexure testing methods to acquire TRS, such as the piston-on-3-balls (PO3B), ring-on-ring (ROR), ball-on-3-balls (BO3B), and ball-on-ring (BOR) methods, require a simple right cylindrical geometry, which can be obtained using traditional powder compaction and sintering techniques and minimal surface preparation. Furthermore, compared to bend bar techniques, the biaxial test method reduces friction between the sample and fixture during testing, improving data accuracy [22]. Currently, ASTM C1499-15 [23] employs the Ring-on-Ring (ROR) method, which tests a larger volume of the sample. However, aligning the test fixture is complex, and the stresses directly under the loading ring are 20 % higher than at the center, potentially causing fractures at the contact ring and invalidating the test [24]. Meanwhile, the ball-on-ring test method enables simple pellet geometries with reduced fabrication time, cost, and waste, with minimal alignment requirements [25]. Hence, the BOR test method is preferred over the ROR standard, as it has proven effective in determining the transverse rupture strength (TRS) in advanced ceramic studies [26].

In this study, CeO2 was doped with TiO2 at varying concentrations (0.1, 0.2, and 0.5 wt %) to determine the optimal doping concentration to improve sinterability, increase grain size, maintain phase stability, and increase fracture strength. The Gd<sup>3+</sup> and Sm<sup>3+</sup> dopants were excluded from the CeO2 matrix to directly compare the effects of the TiO2 sintering aid. Additionally, this study works to establish statistically significant baseline mechanical properties for CeO2 and compare statistical fracture data of TDC with an optimized dopant concentration. The TRS of CeO<sub>2</sub> and 0.1 wt % TDC pellets was determined using a BOR biaxial flexure test method that was previously validated using benchmark ceramics and finite element analysis (FEA) [26]. TRS tests were performed on N > 30 samples for each sample variant to obtain sufficient data for a statistical analysis. A Weibull analysis of TRS data was used to determine the characteristic strength and Weibull modulus. The TRS data were used to establish statistical baseline fracture behavior for CeO<sub>2</sub> and 0.1 wt % TDC and examine the influence of the TiO<sub>2</sub> sintering aid on fracture behavior.

# 2. Methods

# 2.1. $CeO_2$ and TDC pellet fabrication

 $\text{CeO}_2$  and TDC samples were prepared using a 99.9 % purity  $\text{CeO}_2$ powder from Alfa Aesar with an as-received particle size of 14 µm, as stated by the vendor. The powder reference density was estimated to be 7.128 g/cc obtained using a multipycnometer (Quantachrome Instruments, Model SPY-D160E) and used as the reference density for CeO<sub>2</sub>. The composite density of TDC samples from 0.1 to 0.5 wt % TiO<sub>2</sub> was calculated by volume fraction. For TDC samples, TiO2 powder with a 99.7 % purity was obtained from Alfa Aesar. The starting CeO<sub>2</sub> powder and the CeO2 powder with added TiO2 dopant were high energy planetary ball milled (HEPBM) in a zirconia vessel with a 10:1 media (yttria stabilized zirconia) to powder ratio. The powder was milled for 6 h at 250 rpm and 1 h at 500 rpm to disperse agglomerates, reduce particle size and create a homogeneous mixture. Dopant concentrations of 0.1, 0.2, and 0.5 wt % of TiO2 were used to investigate their effect on the CeO2 microstructure (i.e., grain size and sinterability). The HEPBM powder was then mixed with 0.45 wt % Ethylene bis(stearamide) (EBS) binder for 1 h at 150 rpm using YSZ media to improve particle flow characteristics for increased green pellet densities. CeO2 and TDC samples were pressed at 150 MPa in a Carver uniaxial hydraulic press using a dual action die and held for 2 min. The CeO2 and TDC samples used the

same sintering schedule to minimize variables and provide a comparison of sample characteristics under the same sintering parameters. The  $CeO_2$  and TDC samples were sintered at 1600 °C for 4 h with a 4 h binder burnout stage at 300 °C under atmospheric conditions [18].

More than 30 pellets per batch (CeO<sub>2</sub> and TDC) were sintered for TRS tests. The 16 mm diameter sintered pellets were ground parallel to 1.5  $\pm$  0.02 mm in height using 320 grit silicon carbide paper. Sample height was measured using a micrometer with five perimeter and three center measurements, which were averaged to produce the height value used in the TRS calculations.

#### 2.2. Pellet characterization

Powder x-ray diffraction (XRD) (Rigaku Miniflex, 600, Cu k<sub>0</sub>) was performed on as-received CeO2 and the TiO2 dopant powders to verify phase and purity. XRD, with lanthanum hexaboride (LaB<sub>6</sub>) standard (PDF #01-073-1669 [27]) added for line positioning for Rietveld refinement, was also performed on post-sintered samples to investigate changes in phase and lattice parameters. Particle size analysis (PSA) of as-received and HEPBM CeO<sub>2</sub> powder was performed using scanning electron microscopy (SEM) (FEI Teneo) and a laser diffraction system (Horiba LA950). The stoichiometry of the CeO2 pellets was investigated using non-dispersive infrared (NDIR) spectroscopy (LECO, ON836) and electron probe microanalysis (EPMA) (CAMECA, SXFive-TACTICS). Inductively coupled plasma mass spectroscopy (ICPMS) (Thermo Electron Corp., X-Series II Quadrupole) chemical analysis of the HEPBM CeO<sub>2</sub> powder with varying dopant concentrations and their corresponding sintered samples was performed to determine the pre- and post-sintering Ti dopant concentrations in CeO2. ICP-MS metal cation concentration (Ti+) measurements were converted to an oxide basis assuming the Ti + cations formed TiO2. Chemical analysis of pellet cross-sections and surfaces were analyzed using energy dispersive spectroscopy (EDS) (Oxford Instruments Aztec Software) to determine the presence of impurities (i.e., Y, Zr) potentially introduced during the ball milling process or TiO<sub>2</sub> secondary phases in TDC pellets.

The fabricated samples (16 mm diameter x 1.5 mm) were polished to 0.5  $\mu m$  and thermally etched at 1450 °C for 30 min to improve the

visualization of grain boundary relief. The thermally etched samples were imaged using SEM to investigate sample microstructure. Grain size analysis was performed on  $\text{CeO}_2$  and TDC pellets using ASTM standard E112-12 [28] and the average grain size was measured using automated image analysis (ImageJ Software). SEM images of polished cross-sections were used to determine the average porosity of  $\text{CeO}_2$  and 0.1 wt % TDC sintered pellets and measurements were obtained using automated image analysis (ImageJ Software). The theoretical density of sintered samples was obtained using Archimedes density measurements in deionized (DI) water as the immersion fluid.

#### 2.3. Transverse rupture strength test methods

Samples were loaded into a BOR test fixture as seen in the schematic representation in Fig. 1. Samples were centered on the 13 mm diameter ring base using three set screws at a  $120^\circ$  separation. A 3 mm diameter tungsten carbide (WC) loading ball is brazed into the top punch which was vertically aligned using an external sleeve. All samples were loaded at a rate of 0.5  $^{\rm mm}/_{\rm min}$  while collecting force (force indicating accuracy

 $\pm$  0.5%) and displacement data at a sampling rate of 4 Hz. Samples were tested at room temperature and ambient conditions. Force and crosshead displacement data were collected using an 800 series Materials Test System (MTS) test frame. The transverse stress was calculated using the collected force data and Eq. (1) obtained from equibiaxial flexural strength tests of brittle ceramics performed in the literature [25,26, 29–32]:

$$\sigma = \frac{3 \times F}{4 \times \pi \times t^2} \left[ \left( 2(1 + \nu_s) \times \ln \frac{a}{b} \right) + \frac{(1 - \nu_s) \left( 2a^2 - b^2 \right)}{2R^2} + (1 + \nu_s) \right]$$
 (1)

where F is the applied force, t is the specimen thickness,  $\nu_s$  is the Poisson's ratio (0.30) [17] of the test specimen, a is the radius of the support ring (6.5 mm), b is the contact radius of the loading ball (approximated as  $^t/_3$ ), and R is the radius of the test specimen (8.0 mm). The maximum force value for each test was used to calculate the TRS for each tested sample.

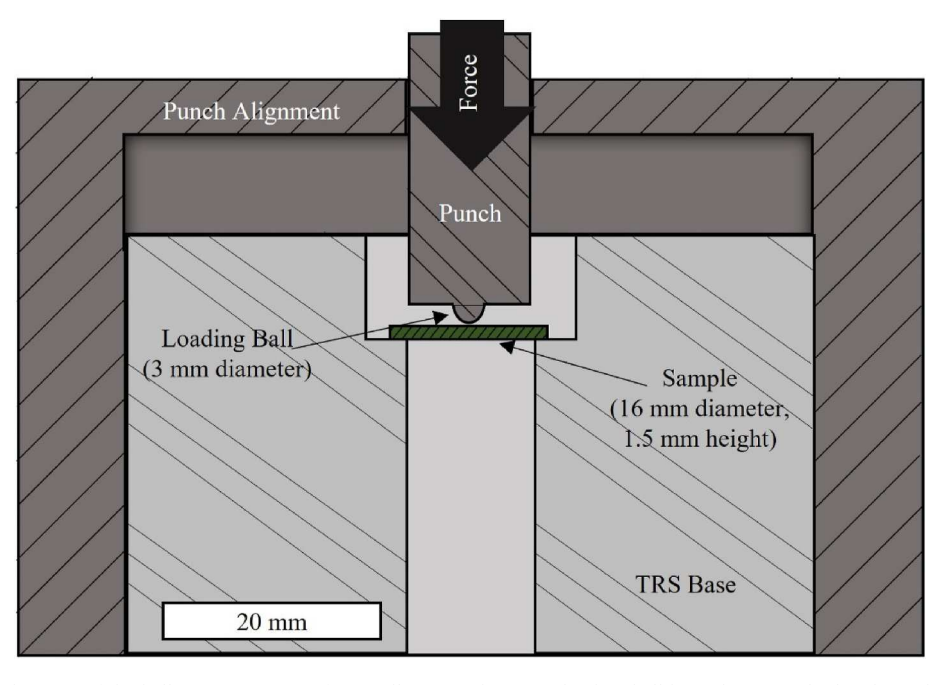


Fig. 1. The cross-section schematic of the ball-on-ring TRS test fixture illustrates the 3 mm loading ball brazed into a cylindrical punch and aligned with an outer sleeve (adapted from Ref. [33]). The force is applied to the loading ball using a rigid push rod attached to a load cell on a mechanical test frame.

#### 3. Results

## 3.1. Powder phase, particle size, and lattice parameter characterization

Powder XRD patterns for the as-received CeO2 and TiO2 powders are shown in Fig. 2. The CeO<sub>2</sub> powder was determined to be phase pure (per the detection limits of the XRD) as it was indexed to match powder diffraction file (PDF) #03-065-2975 [34]. The as received TiO<sub>2</sub> powder diffraction pattern (Fig. 2) resulted in diffraction peaks indicating the presence of rutile and anatase phases (TiO2 polymorphs), PDF #01-073-1669 [35] and PDF #00-02-1272 [36], respectively. Anatase is the metastable phase of  ${\rm TiO_2}$  and predicted to be more stable than rutile when the particle sizes are smaller than approximately 23 nm and is easily transformed to rutile after sintering (>900 °C) [37]. Additionally, the TiO<sub>2</sub> diffraction pattern revealed the presence of a higher order oxide phase (Ti<sub>4</sub>O<sub>7</sub>) that corresponds to PDF #00-077-1390 [38]. The inset image in Fig. 2 shows the first four higher intensity peaks of Ti<sub>4</sub>O<sub>7</sub> are present, where two peaks are shrouded by the highest intensity Anatase peak and two are visible at  $\sim$ 29.5 and 31.6° 20. There are also two lower intensity peaks that were observed at  $\sim$ 45.5° 20. Nonetheless, the small fraction (<1 wt %) present of this higher order phase is not enough to significantly alter doping behavior.

The starting powders used to synthesize CeO<sub>2</sub> and TDC pellets were HEPBM to reduce particle size, break hard agglomerates, and increase pellet sinterability, typically leading to higher density and lower porosity. The same powder processing method was used for CeO<sub>2</sub> and

TDC samples except for the  $TiO_2$  concentrations added to the milling vessel prior to milling. SEM images and PSA indicate the as-received  $CeO_2$  powder had a bimodal distribution at 10  $\mu$ m and 70 nm particles (Fig. 3). After milling the as-received  $CeO_2$  powder, the particle size was reduced to a trimodal distribution at 10  $\mu$ m, 800 nm, and 60 nm particles (Fig. 3). Powder particle size analysis was performed on the HEPBM doped  $CeO_2$  powder which indicated that the particle size was consistent with that of the HEPBM  $CeO_2$  powder in Fig. 3. Although powders were milled for 6 h in a planetary mill and starting particle size (70 nm 10  $\mu$ m) was significantly reduced, powder particle size analysis (Fig. 3) of milled powder shows a trimodal particle size distribution (60 nm, 800 nm, and 10  $\mu$ m), indicating the potential for further reduction in particle distribution and size. A bimodal distribution with a reduction of the 10  $\mu$ m particles could promote greater sample densities.

The XRD patterns for sintered  $CeO_2$  and TDC samples from 0.1 to 0.5 wt %  $TiO_2$  are shown in Fig. 4 and appear to show phase pure  $CeO_2$ . The patterns were indexed to match PDF #03-065-2975 [34], having a typical fluorite crystal structure and no secondary phase formation is observed. This is indicative of the formation of a solid solution. The XRD patterns of the HEPBM powder showed peak broadening from the mechanical milling and like the sintered  $CeO_2$  and TDC samples, they did not exhibit the appearance of any secondary phases. However, due to the low concentration (below XRD detection limits) in TDC samples, the titanium content in the pre-sintered powders and the sintered samples has been measured using ICP-MS, discussed in Section 3.3. EMPA and NDIR spectroscopy of the sintered  $CeO_2$  indicates the O/Ce ratio is 2.00

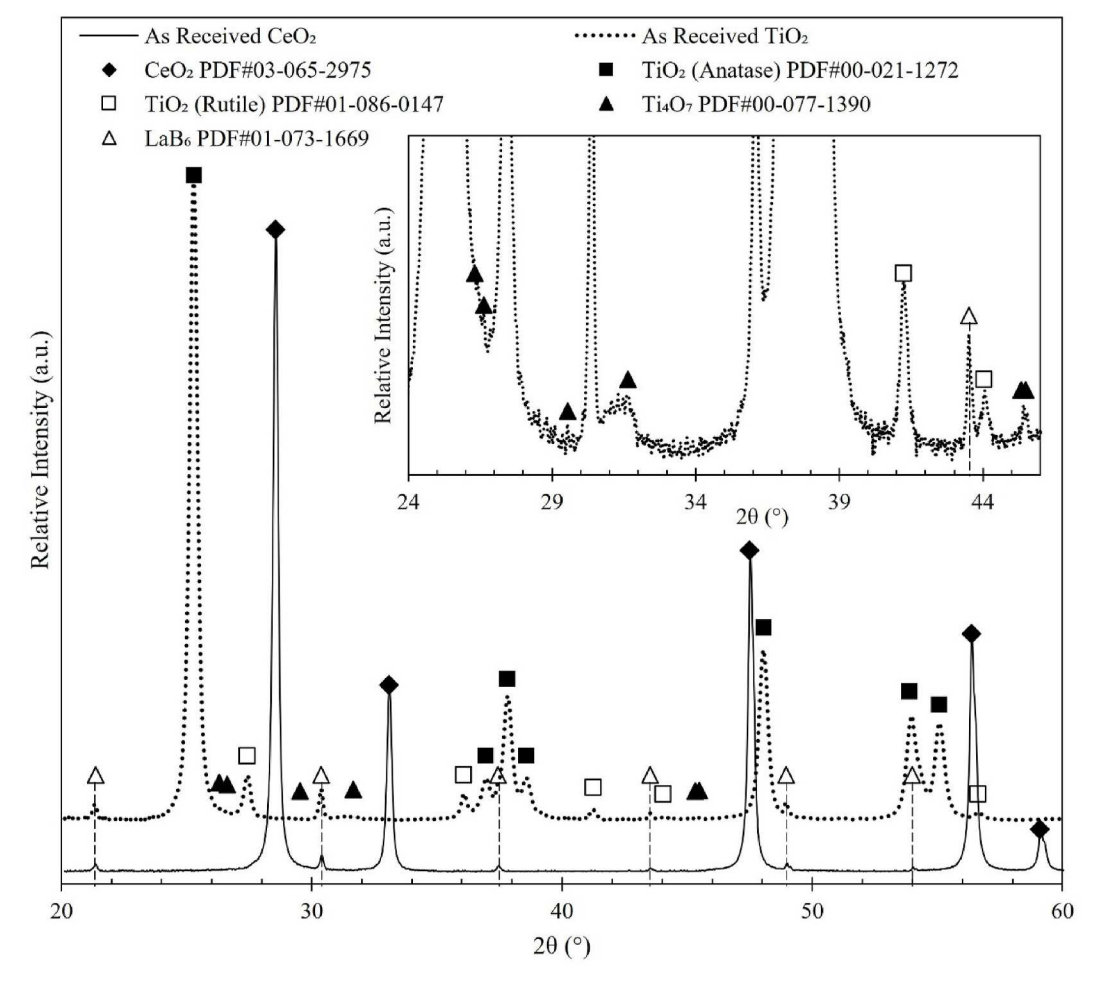


Fig. 2. Powder XRD of the as-received  $CeO_2$  and  $TiO_2$  starting powders. The XRD pattern for the as-received  $CeO_2$  indicates a phase pure starting material. The  $TiO_2$  powder peaks revealed the anatase and rutile polymorphs of  $TiO_2$ . Additionally, small peaks can be seen in the  $TiO_2$  diffraction pattern which correspond to a higher order oxide phase  $Ti_4O_7$ , as seen in the zoomed in  $TiO_2$  pattern in the inset image.

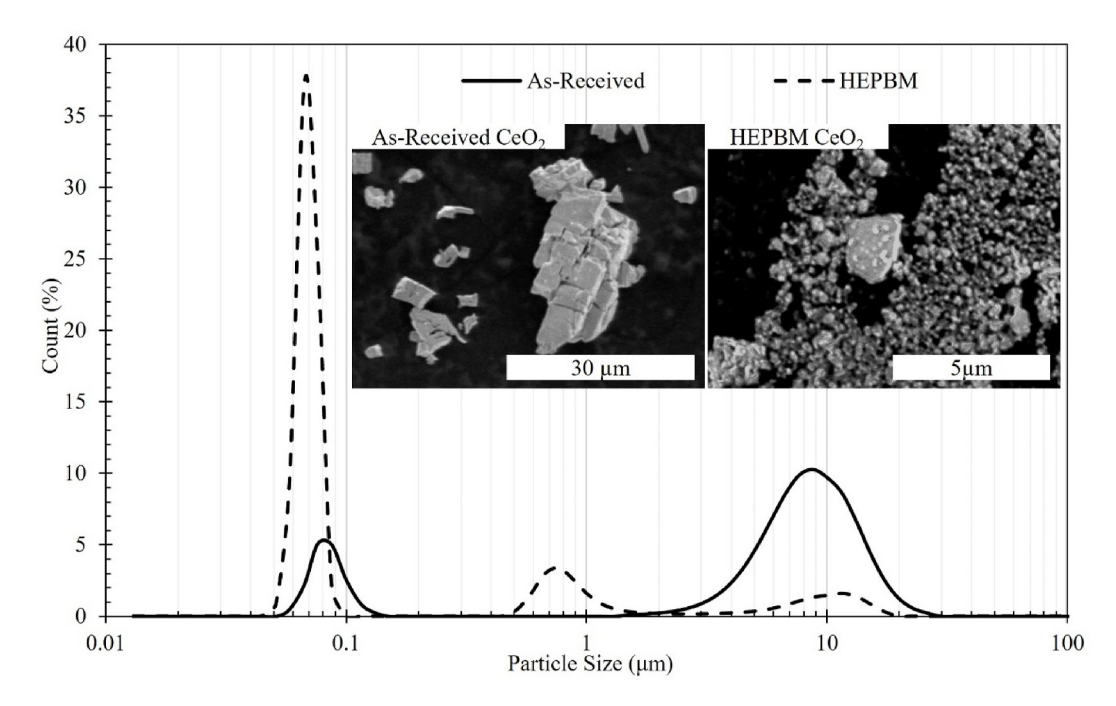


Fig. 3. Particle size analysis of the as-received and HEPBM  $CeO_2$  After HEPBM, the as-received powder was reduced from a bimodal particle size (70 nm and 10  $\mu$ m particles) to a trimodal particle size (60 nm particles, 800 nm, and 10  $\mu$ m particles).

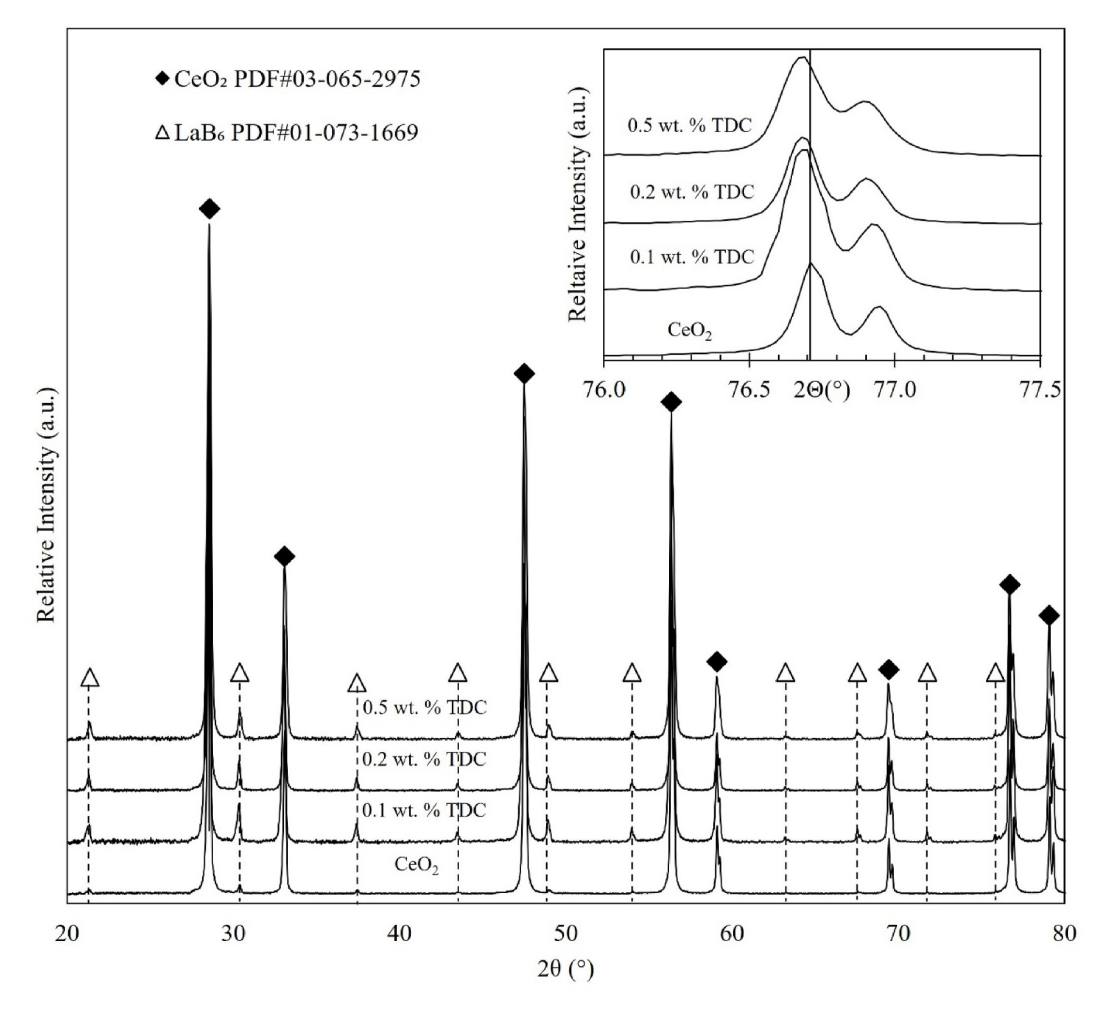
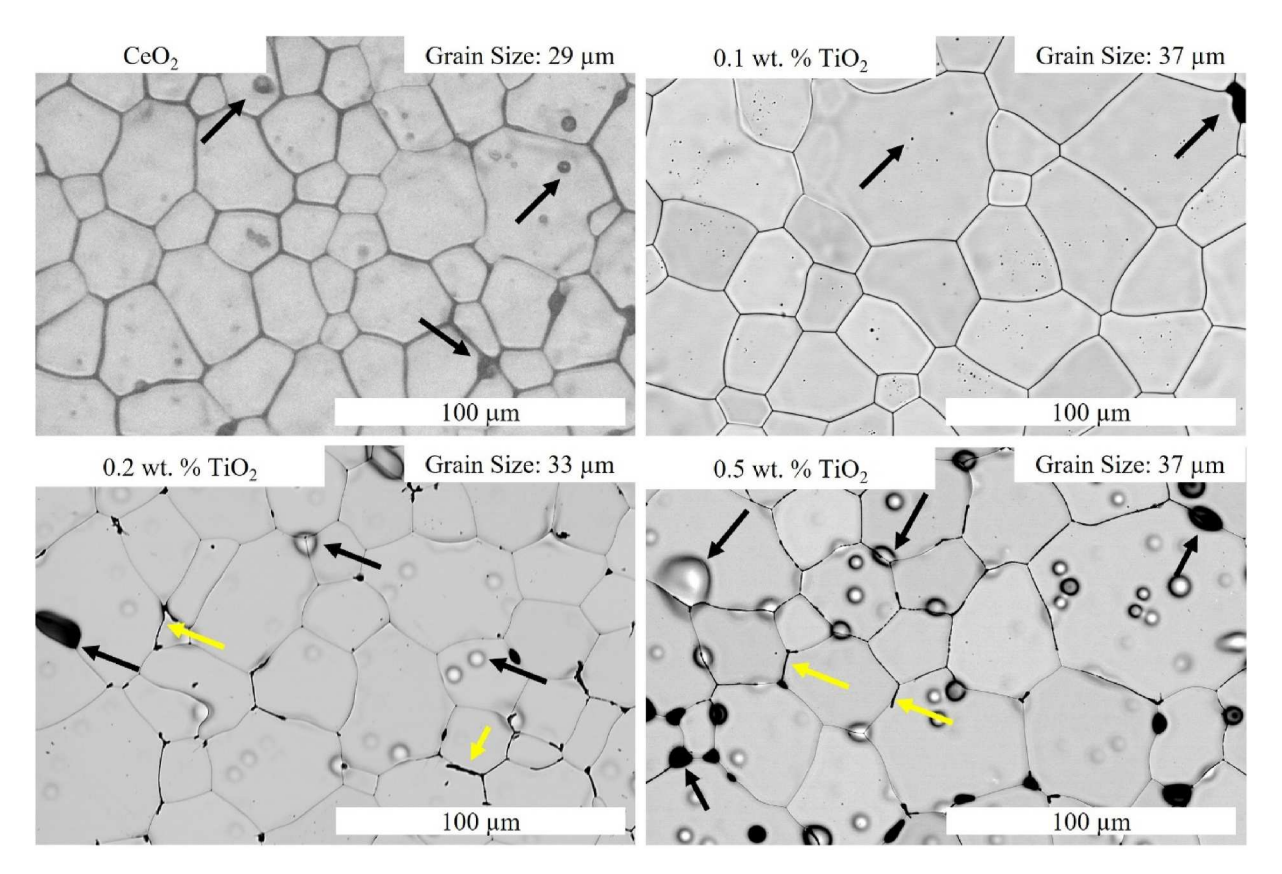


Fig. 4. The CeO<sub>2</sub> and TDC powder diffraction profiles of sintered pellets show shifts in XRD peaks toward lower angles, indicating a lattice expansion. The inset plot shows zoomed in higher angle peaks that clearly demonstrate the diffraction peak shifting for TDC samples to lower 2θ values.



**Fig. 5.** SEM images of thermally etched CeO<sub>2</sub> and TDC pellet cross-sections for dopant concentrations of 0.1, 0.2, and 0.5 wt % TiO<sub>2</sub> sintered at 1600 °C. The black arrows denote pores while the yellow arrows highlight secondary phases in the 0.2 and 0.5 wt % TDC samples. (For interpretation of the references to colour in this figure legend, the reader is referred to the Web version of this article.)

 $\pm$  0.01. The lattice parameter was experimentally determined to be 5.411  $\pm$  0.001 Å and matches what is reported for stoichiometric CeO $_2$  in the literature [34]. NIST standard reference material 660c (LaB $_6$ ) was added to samples to confirm peak positions for CeO $_2$  and TDC powder diffraction patterns as shown in Fig. 4. The XRD patterns for TDC samples show an increase in lattice parameter with increasing dopant concentration (Fig. 4), which is inconsistent with predictions in the literature [39]. The lattice expansion is depicted in the inset image in Fig. 4 where peak shifting of the 0.5 wt % TDC pattern is clearly shifted to lower angles.

#### 3.2. Microstructural characterization

SEM images of thermally etched cross-sections of  $\text{CeO}_2$  and TDC from 0.1 to 0.5 wt % are shown in Fig. 5. Grain size analysis for  $\text{CeO}_2$  and TDC samples was performed using the circular intercept method according to ASTM standard E112-12 and using automated image analysis in ImageJ. The  $\text{CeO}_2$  average grain size was determined to be between 27 and 32  $\mu m$  using ASTM E112-12 and 29  $\pm$  1.16  $\mu m$  using ImageJ analysis. The grain size of TDC samples increased to 37  $\pm$  2.2  $\mu m$  with 0.1 wt % TiO $_2$  addition (solubility limit of TiO $_2$  in CeO $_2$ ) and did not increase with

additional dopant additions. The increase in grain size up to the solubility limit of  $TiO_2$  in  $CeO_2$  has been previously observed in the literature [8,13]. While grain growth was only observed up to 0.1 wt %  $TiO_2$ , further dopant additions decreased sample density and increased surface blistering and small rounded pores within the samples. The small, rounded pores formed within grains and some of the pores coalesced into larger pores along grain boundaries as seen in Fig. 5.

The density of sintered  $CeO_2$  and TDC samples was obtained using Archimedes density measurements, reference and theoretical densities are recorded in Table 1. The density for the 0.2 and 0.5 wt % TDC samples was significantly lower than  $CeO_2$  samples which was likely due to the increased  $CeO_2$  reduction reaction with increasing  $TiO_2$  content [40,41]. The lower density of the 0.2 and 0.5 wt % TDC samples would theoretically reduce their mechanical strength and their lack of sufficient densification preclude them as viable samples for SOFC electrolytes, hence, these samples were excluded from mechanical testing. Areal porosity of the  $CeO_2$  and TDC samples was analyzed from SEM images (Fig. 6) and measurements (Table 1) were obtained using automated image analysis. Large and irregularly shaped pores, as well as larger volumes of porosity create crack initiation points that can greatly reduce the fracture strength of ceramic samples. The 0.1 wt % TDC

Table 1
Archimedes density and grain size analysis for CeO<sub>2</sub> and TDC pellets sintered at 1600 °C in air. Areal porosity was measured using an automated image analysis software (ImageJ) for CeO<sub>2</sub> and 0.1 wt % TDC. Rietveld refinement was performed to determine lattice parameters in GSAS II software and the XRD patterns are shown in Fig. 4.

TiO <sub>2</sub> Concentration (wt. %)	Reference Density (g/cm <sup>3</sup> )	Archimedes Density (% TD)	Grain Size (μm)	Areal Porosity (%)	Lattice Parameter (Å)
0	7.128	$97.4\pm1$	$29\pm1.16$	$3\pm1$	$5.4109 \pm 0.001$
0.1	7.127	$96.6 \pm 1$	$37\pm2.2$	$6\pm1.5$	$5.4128 \pm 0.001$
0.2	7.127	$93\pm0.5$	$33\pm2.64$	$8\pm1.6$	$5.4139 \pm 0.001$
0.5	7.125	$83 \pm 0.5$	$37\pm0.74$	$16\pm3.1$	$5.4146 \pm 0.001$

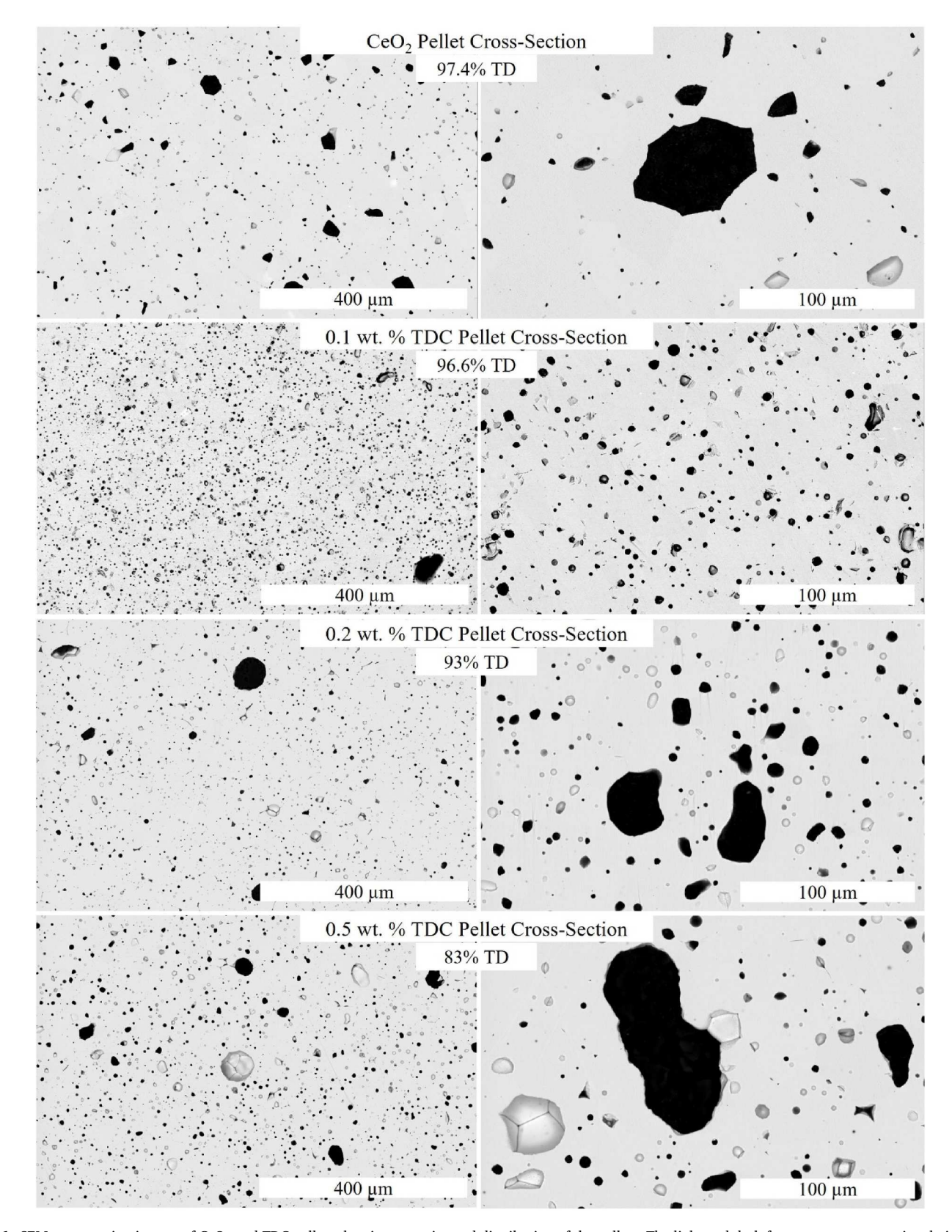


Fig. 6. SEM cross-section images of  $CeO_2$  and TDC pellets showing pore size and distribution of the pellets. The light and dark features are cross-sectional views of pores in the samples.

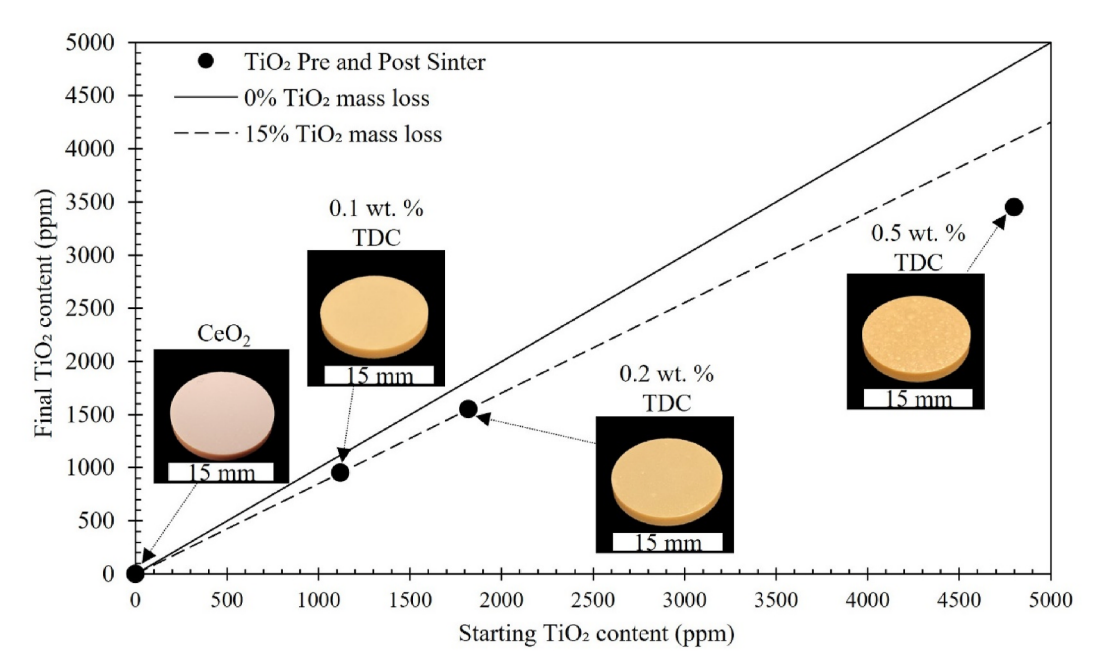


Fig. 7. The data reported in this plot shows the measured TiO<sub>2</sub> doping concentrations of the pre and post sintered TDC samples using ICP-MS. The values are reported in oxide (TiO2) concentrations. The lines represent 0 % volatility (solid line) and 15 % volatility (dashed line).

samples produced samples with a similar density to  ${\rm CeO_2}$  and reduced pore size whereas the 0.2 and 0.5 wt % TDC samples exhibited undesirable densities. Hence, only the 0.1 wt % TDC and  ${\rm CeO_2}$  samples were selected for TRS tests.

## 3.3. Ti content evolution

Doping concentrations in pre-sintered powders and sintered samples are rarely reported in the literature and are of interest due to the volatilization of Ti at the CeO2 sintering temperatures. To the author's knowledge, there are no studies reporting Ti concentrations post sintering in CeO2 and reported additive concentrations overestimate the composition of samples as tested. The solubility limit of Ti in the fluorite crystal structure has been reported to range between  $\approx$ 0.07 and 0.5 wt % between 1400 and 1600 °C [8,42,43]. The wide range of reported solubility limits largely depends on the sintering temperature and atmosphere. As shown in Fig. 7, the volatility of  ${\rm TiO_2}$  during sintering varied between 15 and 30 % for dopant additions between 0.1 and 0.5 wt %. The retention (and incorporation) of Ti atoms within the CeO2 lattice in this work can be confirmed by the lattice parameter expansion with increasing Ti content as shown in Table 1. The TiO2 concentration observed in the 0.5 wt % CeO<sub>2</sub> (≈3400 ppm measured TiO<sub>2</sub>) is lower than the reported solubility limits which could be due to impurity levels or sintering atmosphere. The 0.2 and 0.5 wt % TDC sintered dopant concentrations both exhibit signs of blistering on pellet surfaces and likely exceeded the solubility limit of TiO<sub>2</sub> in CeO<sub>2</sub> in this study (Fig. 7). The excess TiO2 in the 0.2 and 0.5 wt % TDC samples is likely incorporated heterogeneously as a partial solid solution and TiO<sub>2</sub> precipitates and/or a liquid phase along grain boundaries. However, Ti content in the samples is well below the XRD detection limits.

## 3.4. Fracture strength and weibull statistics

Nominally pure, stoichiometric  $CeO_2$  and 0.1 wt % TDC samples were tested using a ball-on-ring test fixture. The 0.2 and 0.5 wt % TDC samples were not TRS tested as the samples resulted in significantly lower densities (93 and 83 % TD) compared to  $CeO_2$  (97 % TD). The maximum transverse tensile stress in the specimen at the maximum force was computed using Eq. (1). The TRS value for each sample was calculated using the maximum force value at failure. The TRS values for  $CeO_2$  ranged from 88 to 160 MPa and from 102 to 171 MPa for the TDC samples (Table 2). Notably, both TRS ranges were consistent with published values in the literature for  $CeO_2$  and doped  $CeO_2$  as shown in Table 3 in the discussion section. The TRS of the 0.1 wt % TDC samples was in the lower range of TRS observed in the literature for doped  $CeO_2$  yet remained within the anticipated values.

This study uses the Weibull distribution of the probability of failure to statistically evaluate the likelihood of brittle fracture for both sample sets. An appropriate Weibull analysis requires a data set with a sample size of  $N \ge 30$  that exhibits a linear fit and assumes that 1) flaws do not interact, and 2) the structure fails when a single flaw becomes critical. Equation (2) highlights the relationship between the probability of failure ( $P_f$ ), characteristic strength ( $\sigma_0$ ), Weibull modulus (m), and fracture strength ( $\sigma_f$ ), where  $\sigma_f$  is the measured TRS [26,44].

$$lnln\left(\frac{1}{1-P_f}\right) = m * ln \left[\sigma_f\right] - m * ln \left[\sigma_0\right]$$
 (2)

Weibull parameters (m and  $\sigma_0$ ) were extracted for  $CeO_2$  and 0.1 wt % TDC sample sets using Equation (2) and a linear regression fit to the data. The Weibull modulus, m, is determined by the slope of the line representing the plotted TRS values and offers insight into the scatter of fracture data. A material with a higher m (dimensionless) value indicates

**Table 2**Weibull statistics for CeO<sub>2</sub> and TDC TRS samples.

Sample Type	TRS (MPa)	Characteristic Strength $[\sigma_0]$ (MPa)	Weibull Modulus [m]	Regression Fit [R <sup>2</sup> ]	# of Samples
CeO <sub>2</sub>	88–160	128	8.5	0.96	33
TDC	102–171	151	9.3	0.97	31

Table 3
Fracture data and sample characteristics for this study and values found in the literature for CeO<sub>2</sub> and doped CeO<sub>2</sub> samples.

Ref.	Material	Density (%TD)	Grain Size (µm)	TRS (MPa)	Weibull Modulus [m]	# of Tests	Test Method <sup>a</sup>
CeO <sub>2</sub>							
This study	CeO <sub>2</sub>	97 %	29	129	8.5	33	BOR
[54]	$CeO_2$	99 %	4	250	_	5	POR
[55]	CeO <sub>2</sub>	98 %	_	139	_	5	3-PB
[56]	CeO <sub>2</sub>	97 %	_	140-155	_	_	4-PB
[57]	CeO <sub>2</sub>	80 %	11	75-82	_	2	4-PB
[47]	CeO <sub>2</sub>	94–96 %	24	113	_	5	4-PB
[58]	$CeO_2$	96 %	-	138	_	1	4-PB
Doped CeO <sub>2</sub>							
This study	Ti <sub>0.001</sub> Ce <sub>0.999</sub> O <sub>2</sub>	96 %	37	150	9.3	31	BOR
[56]	$Gd_{0.15}Co_{0.005}Ce_{0.845}O_2$	99 %	2	497	3.6	9	BO3B
[54]	$Gd_{0.1}Ce_{0.9}O_2$	99 %	1.25	175-250	_	5	POR
[54]	$Y_{0.1}Ce_{0.9}O_2$	99 %	1.25	150-175	_	5	POR
[54]	$Sm_{0.1}Ce_{0.9}O_2$	99 %	1.25	160-245	_	5	POR
[59]	Gd <sub>0.1</sub> Ce <sub>0.9</sub> O <sub>1.95</sub>	99 %	2	150	_	5	PO3B
[60]	$Gd_{0.2}Ce_{0.8}O_2$	94 %	_	210	_	20	3-PB
[61]	$Gd_{0.1}Ce_{0.9}O_2$	_	_	150	_	17	4-PB
[62]	Sm <sub>0.2</sub> Ce <sub>0.8</sub> O <sub>1.9</sub>	86-98 %	10-20	53-81	9.09	8	4-PB
[58]	$Gd_{0.2}Ce_{0.8}O_2$	96 %	_	143	_	10	4-PB

<sup>&</sup>lt;sup>a</sup> Ball-on-ring (BOR), Piston-on-ring (POR), Ball-on-3 ball (BO3B), Piston-on-3 ball (PO3B), 3-point bend (3-PB), and 4-point bend (4-PB).

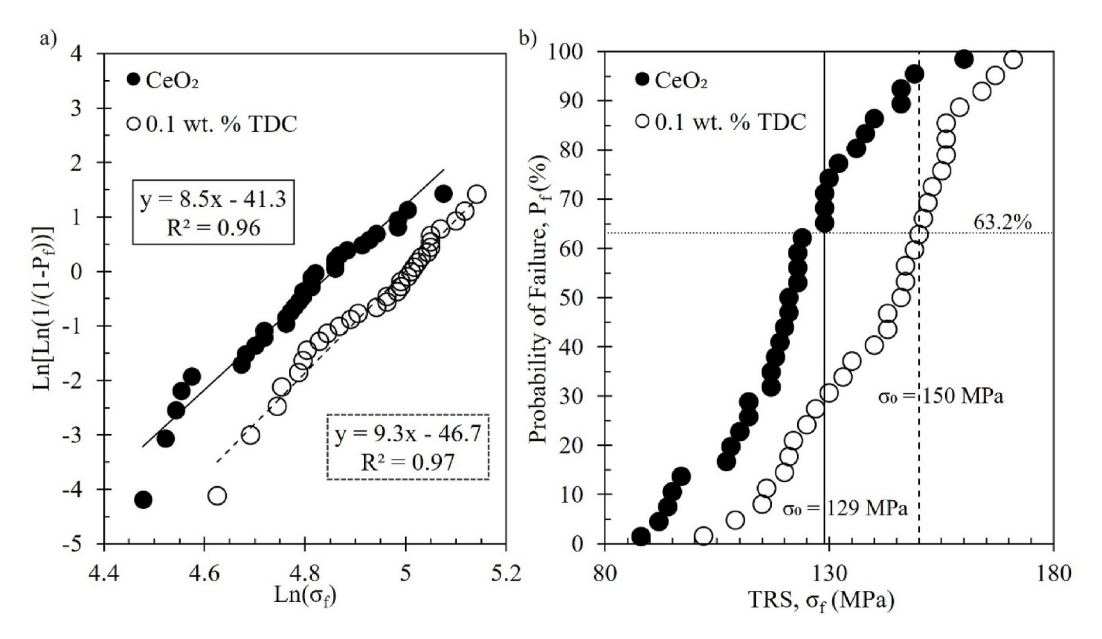


Fig. 8. The statistical analysis for CeO2 and 0.1 wt % TDC is shown in a) the Weibull plot and b) the probability of failure plot.

increased material reliability and a greater level of consistency among samples [45]. The coefficient of determination ( $\mathbb{R}^2$  value) for the linear regression fit of  $\text{CeO}_2$  and 0.1 wt % TDC fracture data were approximately 96 % and 97 %, respectively. The slope of the linear fit lines, representing m, are 8.5 and 9.3  $\text{CeO}_2$  and 0.1 wt % TDC (Fig. 8[a]), respectively. The characteristic strength was extracted where the probability of failure ( $P_f$ ) is equal to 63.2 %, as illustrated in Fig. 8[b]. The characteristic strength of the  $\text{CeO}_2$  and TDC samples are 128 MPa and 151 MPa, respectively. The lack of data exhibiting deviations from a linear fit strongly suggests that the fracture behavior of the specimens is well-suited to an analysis using the Weibull distribution function. Summarized Weibull parameters and average TRS values for the  $\text{CeO}_2$  and 0.1 wt % TDC data sets can be found in Table 2.

## 3.5. Fractography

The loading ball contact zone, tensile surface, and fracture surfaces

were examined to determine fracture modes and origin. Fig. 9 shows the fracture mode for the  $\text{CeO}_2$  and 0.1 wt % TDC pellets.  $\text{CeO}_2$  fracture surfaces displayed a mixture of intergranular (occurring along grain boundaries) and transgranular (occurring through grains) fracture. Meanwhile, the fracture mode of the 0.1 wt % TDC pellets was predominantly transgranular with small pores both within grains and along grain boundaries. The  $\text{CeO}_2$  samples exhibited significantly less blistering on the surface and formation of pores within the bulk and instead showed larger, irregularly shaped pores along grain boundaries.

Full fracture surfaces were imaged to show Hertzian contact damage (compressive surface) as well fracture initiation points (tensile surface), which were observed in all of the fractured pellets and is shown in the representative surface images of Figs. 10 and 11. The Hertzian damage is presumably caused by the loading ball due to the fact that the applied force generated Hertzian contact stresses surpassing the hardness of  $\text{CeO}_2$  ( $\approx$ 4 GPa HV) [46]. Fig. 12 shows a representation of theoretical Hertzian contact stress versus transverse stress, generated by a 3 mm

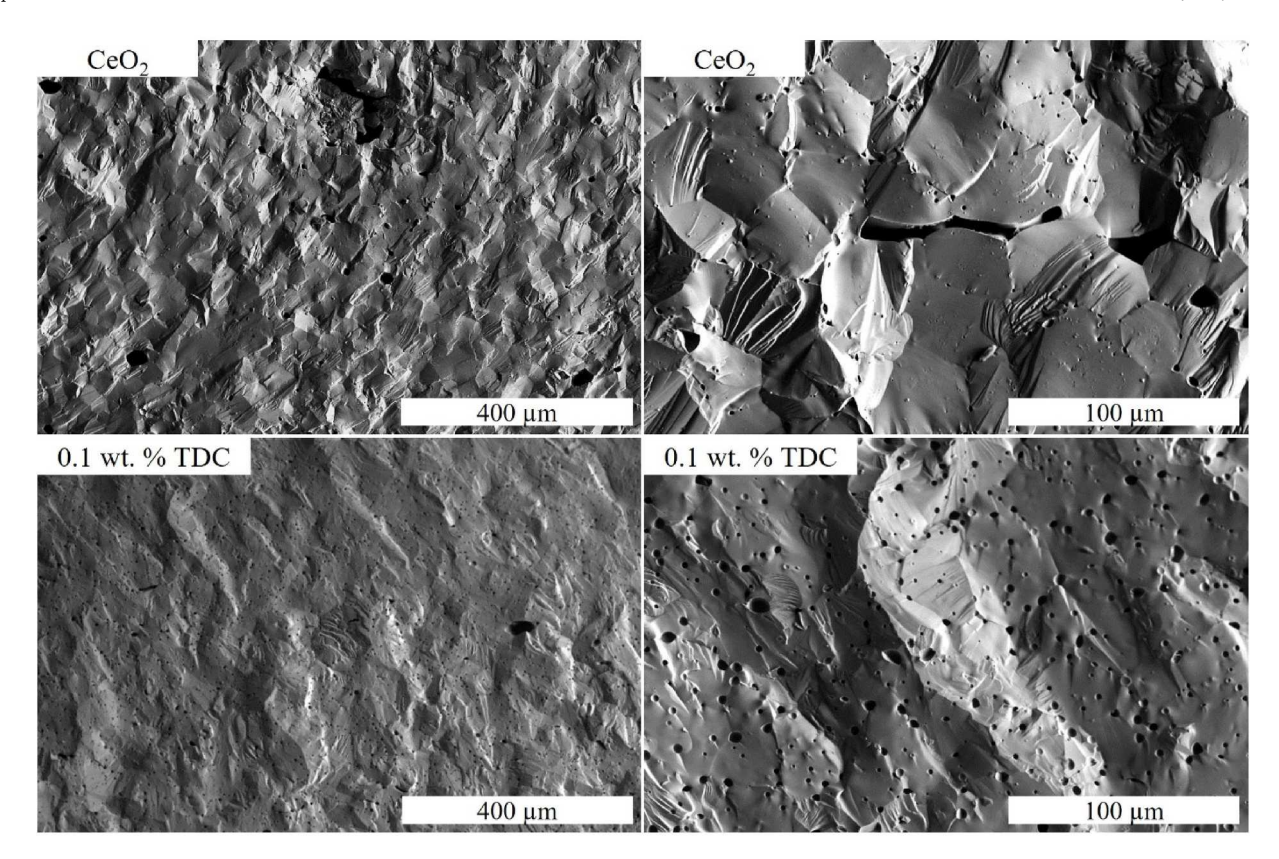


Fig. 9. SEM fracture surfaces images of  $CeO_2$  and 0.1 wt % TDC pellets indicate that  $CeO_2$  pellets exhibited primarily intergranular fracture while TDC pellets primarily displayed transgranular fracture.

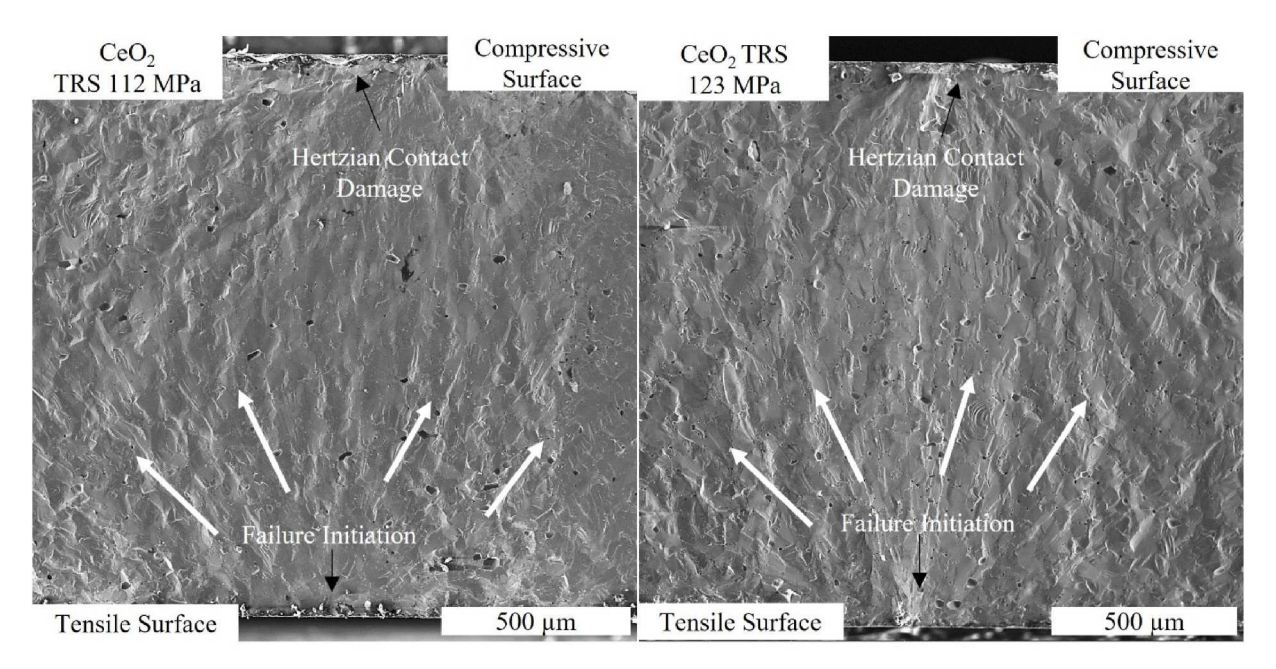


Fig. 10. Fracture surface images of two CeO<sub>2</sub> pellets that show signs of Hertzian contact damage on the compressive surface, near the loading ball contact region. Failure initiation occurred on the tensile surface near the highest region of stress concentration. Fracture surfaces appear to be more uneven or faceted than those of 0.1 wt % TDC fracture surfaces.

loading ball during TRS testing of  $CeO_2$  and 0.1 wt % TDC samples with a thickness of 1.5 mm. Despite the presence of Hertzian contact damage, it appears that failure initiation originated from the center of the pellets on their tensile surfaces, suggesting that the samples failed in tension.

#### 4. Discussion

## 4.1. Structure and defect behavior in CeO2 and TDC samples

Establishing the baseline fracture data for  ${\rm CeO_2}$  necessitates a stoichiometric, single phase  ${\rm CeO_2}$  test material. XRD analysis of  ${\rm CeO_2}$ 

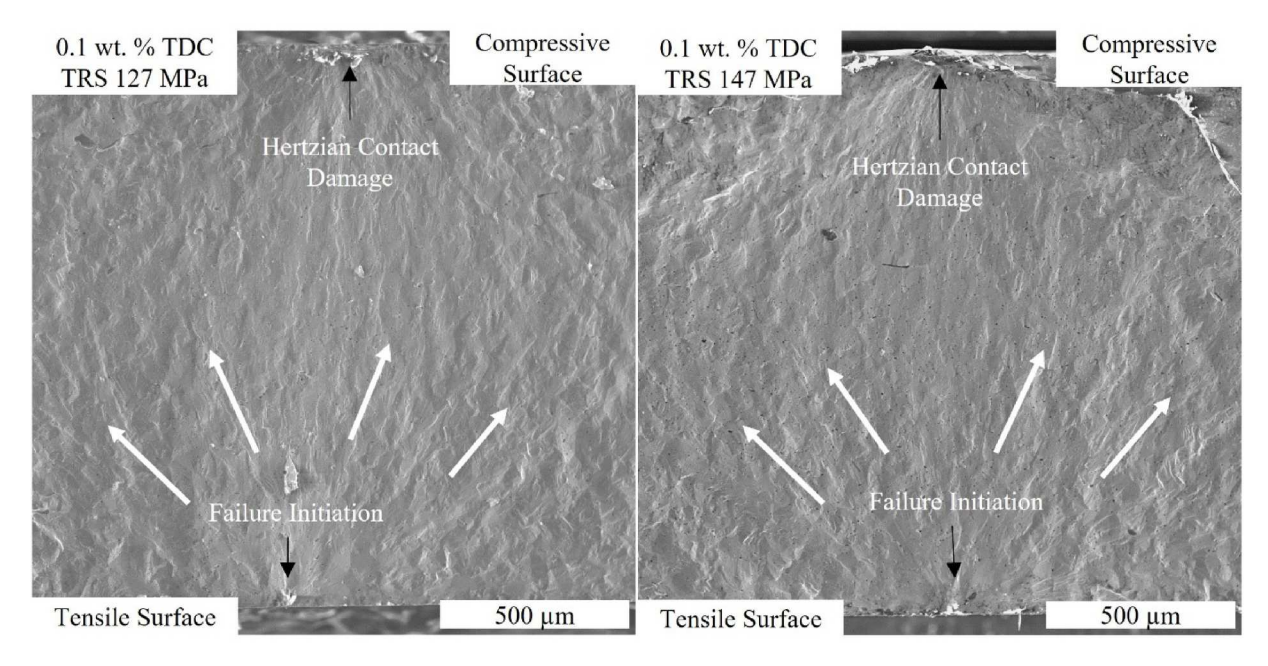


Fig. 11. Fracture surfaces of two 0.1 wt % TDC pellets that show signs of Hertzian contact damage on the compressive surface, near the loading ball contact region. Failure initiation occurred on the tensile surface near the highest region of stress concentration. The fracture surfaces are smoother and are indicative of transgranular fracture.

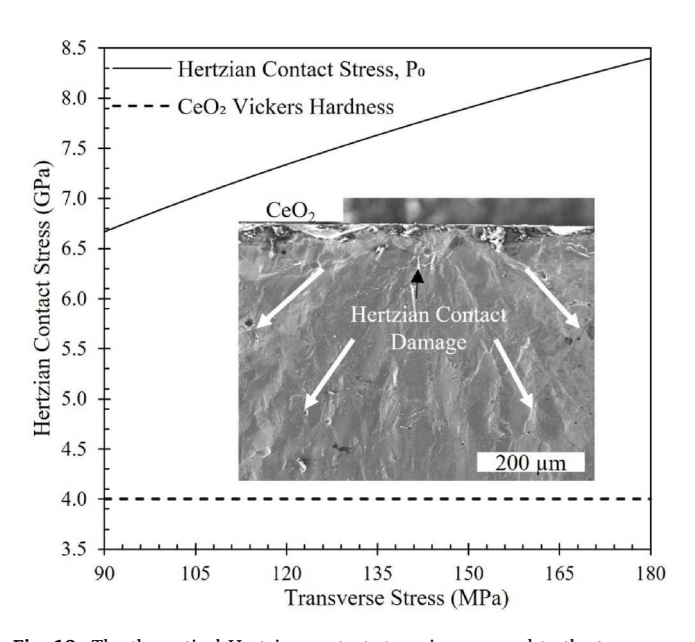


Fig. 12. The theoretical Hertzian contact stress is compared to the transverse stress (from lowest TRS to highest TRS) in a 1.5 mm pellet thickness for applied loads using a 3 mm diameter WC loading ball. The Hertzian contact stress produced by the loading ball exceeds the Vickers hardness ( $\approx$ 4 GPa) [46] for all CeO<sub>2</sub> and TDC TRS tests.

indicates samples have a single CeO $_2$  phase with a lattice parameter matching the typical value published in the literature. Additionally, EMPA and NDIR spectroscopy indicate the O/Ce ratio is  $2.00\pm0.01$  which agrees with a stoichiometric CeO $_2$ . The formation of Ce $_2$ O $_3$  in the CeO $_2$  matrix was of concern, as CeO $_2$  can readily reduce to Ce $_2$ O $_3$  when sintering at higher temperatures. The formation of Ce $_2$ O $_3$  would cause a lattice expansion and detrimentally influence fracture behavior as reported in previous studies [47]. However, given the phase purity and stoichiometry of the CeO $_2$  pellets, the samples were deemed appropriate to establish a TRS benchmark data set for CeO $_2$ .

Although the TDC powder diffraction patterns did not exhibit the presence of any secondary phases, there is a diffraction peak shift towards lower 2θ values in all TDC samples as compared to CeO<sub>2</sub> (Fig. 4). This diffraction peak shift indicates an increase in the lattice parameter and is accentuated with an increased Ti concentration as reported in Table 1. This finding contrary to theoretical behavior as Ti<sup>4+</sup> (0.74 Å)/  $Ti^{3+}$  (0.67 Å) is predicted to sit on  $Ce^{4+}$  (0.97 Å) lattice sites which would theoretically decrease the lattice due to their small ionic radii [8, 39]. However, a CeO<sub>2</sub> lattice expansion has been shown in previous studies using undersized dopant cations such as Mn and Mg [48,49]. The authors' feel there are two possible explanations for the expansion of the lattice parameter: First, the redox potential for Ti<sup>4+</sup> to Ti<sup>3+</sup> at the sintering temperature used to fabricate the samples is nearly zero [50]. Hence, it is possible that some of the titanium are sitting in interstitial sites of the CeO<sub>2</sub> matrix as Ti<sup>3+</sup> in conjunction with a balance of titanium sitting on Ce lattice sites as Ti<sup>4+</sup>. The substitutional/interstitial balance would create Ce vacancies and increase cerium diffusivity due to a Ce cation vacancy diffusion mechanism [51]. Interstitial titanium would be favorable due to its small ionic radius compared to Ce<sup>4+</sup> and lead to a lattice expansion and compressive residual stresses. The second possible explanation is that Ti4+ atoms sit on Ce lattice sites and due to their significantly smaller radii, some of the  $Ce^{4+}$  ions reduce to  $Ce^{3+}$  to compensate for the large lattice distortions [13]. Alternatively, Ti<sup>4+</sup> can sit on Ce lattice sites and reduce Ce<sup>4+</sup> to Ce<sup>3+</sup> by intervalence charge transfer [50]. In either case, the reduction of Ce<sup>4+</sup> to Ce<sup>3+</sup> would lead to oxygen vacancies and an increase in lattice parameter. The distorted lattice and increased oxygen vacancies can apparently lead to an enhanced cation interstitial diffusion mechanism [13]. Both explanations would lead to 1) an increase in lattice parameter and 2) an increase in Ce diffusivity which would increase grain boundary mobility (i.e., grain growth), which was observed. However, the substitutional Ti<sup>4</sup> on Ce lattice sites leading to the reduction of Ce<sup>4+</sup> to Ce<sup>3+</sup> is more commonly referred to in the literature for a solid solution of Ti in CeO<sub>2</sub>.

In this study, the 0.1 wt % TDC samples, which had a larger lattice parameter compared to  $CeO_2$ , resulted in a TRS that was 20 MPa higher than  $CeO_2$ . Hence, it is likely that the lattice expansion is producing compressive residual stresses in the lattice, likely promoting an increased fracture strength. The evolution of  $TiO_2$  from the  $CeO_2$  matrix

during sintering was to be expected as  $TiO_2$  has a higher vapor pressure than  $CeO_2$ . Additionally, other studies [52] incorporating Ti dopants into oxides report the formation of small, round pores when exceeding the solubility limit, which was observed in all TDC samples. It is probable that a portion of the  $Ti^{4+}$  was reduced to  $Ti^{3+}$  during sintering as ICP-MS measured approximately a 15 %  $TiO_2$  mass loss from the 0.1 and 0.2 wt % TDC samples while the 0.5 wt % TDC sample exhibited a mass loss of about 28 %  $TiO_2$ . The greater Ti content that evolved from the 0.5 wt % TDC sample helps to explain the marked difference in surface morphology (blistering) and round void formations that are likely attributed to the formation and evolution of Ti from the pellet. Although ICP-MS show 0.5 TDC evolved a greater percentage of stating dopant, the samples also had the greatest final concentration of Ti dopant and is likely responsible for the greater expansion in lattice parameter.

For all TDC samples, the lattice parameter increased with doping concentration, but the grain size did not increase beyond 37  $\mu m$  for all doping concentrations. Only the 0.1 wt % TDC samples resulted in pellets with a desirable density and surface morphologies, and the lattice parameter increased by only 0.002  $\pm$  0.001 Å. Additionally, secondary phases were not observed, a beneficial outcome as secondary phases can detrimentally impact SOFC performance. The absence of secondary phases was expected as a previous study [13] focused on grain growth and densification of CeO2 suggested a doping limit near 0.1 mol % TiO2 ( $\approx$ 0.08 wt % TiO2) to avoid the formation of secondary phases and increase grain boundary mobility. Hence, sample fabrication for TRS tests focused on CeO2 and 0.1 wt % TDC pellets.

#### 4.2. Transverse rupture strength

In this study, the fracture behavior of CeO $_2$  was assessed in comparison to 0.1 wt % TDC using a BOR fixture (Fig. 1) that had been previously validated via experimental and numerical analyses [26]. Studies have primarily investigated the TRS of CeO $_2$  and doped CeO $_2$  using bend bar flexure techniques (Table 3) with limited samples (typically N  $\leq$  5), leading to considerable statistical variance. Nevertheless, in all studies examining fracture data of doped CeO $_2$ , the number of samples used was limited to ten or fewer, except for two studies that used a maximum of 20 samples. As such, the limited sample numbers preclude the acquisition of important statistical fracture data, such as the Weibull modulus and characteristic strength.

With over 30 samples tested in each material system, this study obtained sufficient fracture data to determine Weibull parameters for CeO2 and 0.1 wt % TDC. The 0.1 wt % TDC samples were expected to have a higher density than CeO2 due to the TiO2 sintering aid but resulted in a slightly lower density ( $\approx$ 1 %). Due to the lower density of the 0.1 wt % TDC samples, it was anticipated that the CeO2 samples would exhibit equal or superior fracture strength performance compared to the 0.1 wt % TDC samples. Although a larger grain size in TDC samples was desirable to reduce grain boundary resistance and increase overall conductance, the smaller grain size in the CeO2 samples should contribute to an increased fracture strength if the samples follow the Orowan-Petch relationship [53]. Contrary to expectations, TRS results (Fig. 8[a, b]) revealed the 0.1 wt % TDC samples exhibited an increased characteristic strength and Weibull modulus, despite having a larger average grain size and increased porosity. This increase in Weibull parameters suggests that the TiO2 sintering aid not only enhanced fracture strength by a little over 16 % but also contributed to a reduction in the variability of fracture strength. In other words, critical flaws that initiate fracture were more consistent from sample to sample, thereby reducing variability in fracture strength. The TiO2 sintering aid resulted in increased fracture strength with less variability for the 0.1 wt % TDC samples and fractography was performed to gain insight into the TRS results (discussed in section 4.3).

The 0.1 wt % TDC samples exhibited an apparent solid-solution microstructure whereas  $TiO_2$  additions that significantly exceed their solubility limit in  $CeO_2$  form numerous precipitates that can inhibit

grain growth by pinning grains [12]. These precipitates form secondary phases that may toughen the material and increase fracture strength; however, the formation of these secondary phases in doped  $CeO_2$  may form low conductance phases that reduce overall conduction [12]. Therefore, optimizing the addition of the  $TiO_2$  sintering aid in doped  $CeO_2$  to increase density and grain size while maintaining a solid-solution microstructure is of interest to increase fracture strength while enhancing electronic conductance.

Finally, it is important to note that, in line with statistical fracture theory, increasing the effective test volume increases the likelihood of probing a larger critical flaw, thereby reducing fracture strength. The characteristics of TRS test samples have been investigated and documented, along with essential test parameters necessary for a comprehensive comparison with alternate flexure test methods. Geometric dimensions of the test fixture provide the required data for effective volume calculations, critical for comparing different sample geometries and test configurations.

## 4.3. Fracture surface analysis

Ceramic fracture is largely based on the weakest link theory, wherein the largest critical flaw which interacts perpendicularly to the applied stress field will initiate crack propagation. The likelihood of fracture initiation at a lower stress increases with larger or sharper flaws in the material (i.e., micro-cracks from processing, inclusions, pores). Consequently, the pore size, distribution, and geometry impact fracture behavior [63] and should be characterized. The pore size and distribution of polished cross-sections for both CeO2 and 0.1 wt % TDC samples (depicted in Fig. 6) were estimated using ImageJ. The results from the image analysis revealed that, despite a slightly higher density, the CeO<sub>2</sub> samples have a higher number of large pores, with the maximum measured pore size of approximately 83  $\mu m$ , compared to the 0.1 wt % TDC pellets. The 0.1 wt % TDC pellets have a more homogenous pore size distribution and a reduced presence of larger pores, with a maximum measured pore size of approximately 75  $\mu m$ . The greater quantity of large pores present in the CeO<sub>2</sub> samples is evident in Fig. 6. A higher frequency of large pores increases the likelihood that the applied stress field will interact with one of the larger pores, leading to failure. Therefore, the analysis of flaw size and distribution, in this context, pores, provides critical data that informs TRS and fracture behavior such as fracture modes.

SEM images of fracture surfaces in Fig. 9 indicate that the fracture modes in  $\text{CeO}_2$  exhibited a mixed pattern of transgranular and intergranular fracture, with a more pervasive intergranular fracture mode. Fig. 9 indicates that the fracture mode for the 0.1 wt % TDC pellets was predominantly transgranular with minimal intergranular fracture. Previous studies on the fracture mode of  $\text{Al}_2\text{O}_3$  have suggested that grain size can influence fracture mode, with smaller grain sizes tending to favor intergranular fracture [64]. However, in the context of this study, involving  $\text{CeO}_2$  and 0.1 wt % TDC pellets, the difference in average grain size does not adequately account for the difference in fracture modes. A more detailed examination of the pore geometry and location provided additional insights into the observed differences in fracture mode.

In the  $CeO_2$  samples, the presence of intergranular fracture facilitates the identification of pores located along grain boundaries as indicated by the arrows in Fig. 13[a]. When compared with pores in the 0.1 wt % TDC pellets shown in Fig. 13[b], it is notable that the pores along grain boundaries in the  $CeO_2$  pellets generally exhibit a geometry with a larger radius of curvature, acting as stress concentrators in the applied stress field. This characteristic is exemplified by the pore marked by the yellow arrow in Fig. 13[a]. The higher stress concentrations from pores along grain boundaries in  $CeO_2$  potentially lead to weakening of the grain boundaries. The 0.1. wt. % TDC pellets exhibit a predominantly transgranular fracture mode, although pinpointing the location of pores along grain boundaries proves challenging. We hypothesize the pore size and geometry along the  $CeO_2$  grain boundaries influenced the

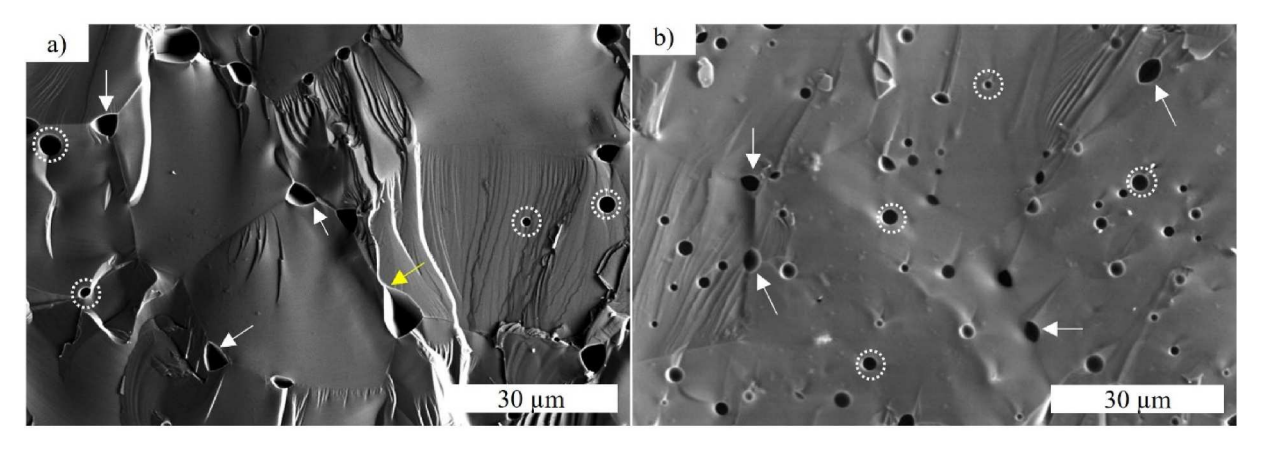


Fig. 13. The SEM images show pore and pore geometry, as indicated by the arrows, in a) CeO<sub>2</sub> and b) 0.1 wt % TDC. Additionally, examples of pores from gaseous bubble formations are highlighted by the dashed circles.

predominantly intergranular fracture mode as compared to the more rounded pores in the 0.1 wt % TDC samples [65].

In addition to the size, geometry, and location of pores analyzed in fractographic examinations, the presence of small spherical pores was noted, and their prevalence appeared to increase with the addition of TiO<sub>2</sub>. The increased formation of spherical pores in the 0.1 wt % TDC samples, presumed to be gaseous bubbles primarily trapped within grains. The authors speculate that the formation of the gaseous bubbles is attributed to either the CeO2 reduction reaction [40,41] or the evolution of TiO2 from the sample during the sintering process. The use of TiO<sub>2</sub> as a sintering aid in MgAl<sub>2</sub>O<sub>4</sub> has shown to increase porosity, likely due to the formation of bubbles [66]. The authors hypothesize that the formation of small round pores occurs with the decomposition of the starting Al(OH)<sub>3</sub> and MgO to form point defects induced by the TiO<sub>2</sub> [66]. The study concluded that the higher apparent porosity samples with smaller, more homogenous pores ultimately resulted in an increased fracture strength [66]. Lastly, a numerical study using the cohesive zone model for fracture propagation in polycrystalline materials can help to explain the competing intergranular and transgranular fracture modes observed in the CeO2 and 0.1 wt % TDC samples. The numerical study concluded that transitions from transgranular to intergranular fracture can be attributed to crystal orientation accommodation where some grains are oriented such that they are more susceptible to cleavage across the grain [67]. Therefore, for the CeO<sub>2</sub> samples in this study, we hypothesize that fracture propagates along weakened grain boundaries except when encountering grains that are favorably oriented for cleavage microcracking, leading to a mixed fracture mode.

Finally, in all  $CeO_2$  and TDC fracture surfaces, Hertzian contact damage was observed and is attributed to compressive stresses produced by the loading ball which exceed the hardness of  $CeO_2$ . Despite the presence of Hertzian contact damage all sample failures originated on tensile surfaces, confirming the validity of the tests. Additionally, Hertzian contact damage has been observed using the BOR test method for  $UO_2$  pellets in previous work, but it was shown that the Hertzian contact damage has little to no effect on the measured fracture strength [33]. Considering that  $CeO_2$  is frequently used as a surrogate for  $UO_2$  due to its similar chemical, thermophysical, and structural properties [68], the authors feel sufficiently confident that the observed contact damage did not influence fracture strength of both  $CeO_2$  and 0.1 wt % TDC pellets.

# 5. Conclusion

This study focused on the fabrication and characterization of  $\text{CeO}_2$  and doped  $\text{CeO}_2$  samples with varying  $\text{TiO}_2$  concentrations (0.1, 0.2, and 0.5 wt %).  $\text{CeO}_2$  samples were doped with  $\text{TiO}_2$  as a sintering aid, aiming

to enhance density and grain size of  $CeO_2$  for applications in IT-SOFCs. Additionally, TRS data were obtained for  $CeO_2$  and 0.1 wt % TDC pellets with a robust data set (N > 30) to perform a statistical analysis and extract Weibull parameters, which have been lacking in the literature. This study can be summarized with the following conclusions.

- 1. All  ${\rm TiO_2}$  dopant concentrations used in this study enhanced the grain size of TDC pellets when compared to  ${\rm CeO_2}$  (grain size increased from 29 to 37  $\mu$ m). However, concentrations greater than 0.1 wt % did not further increase the grain size and notably reduced sample density and increased areal porosity.
- 2. Diffraction patterns for all samples did not reveal secondary phases but there was a diffraction peak shift to lower 2θ values in TDC samples, corresponding to a lattice expansion which was accentuated by Ti content additions. The lattice expansion is likely associated with compressive residual stresses that facilitated a higher fracture strength.
- 3. The incorporation of Ti into the  $CeO_2$  lattice is proposed to occur as  $Ti^{4+}$  atoms sitting on Ce lattice sites with the reduction of surrounding  $Ce^{4+}$  to  $Ce^{3+}$ , promoting oxygen vacancies and lattice expansion.
- 4. ICP-MS measurements revealed that there is a TiO<sub>2</sub> mass loss during sintering of approximately 15 % for 0.1 and 0.2 wt % TDC, a figure that nearly doubled to 28 % for 0.5 wt % TDC. Hence, studies that only report powder additive concentrations overrepresent the composition of final sintered samples due to the volatility of reduced TiO<sub>2</sub> at sintering temperatures.
- 5. The  $CeO_2$  and 0.1 wt % TDC samples had a similar density with an average grain size of 27 and 37  $\mu$ m, respectively. The 0.1 wt % TDC samples had a higher Weibull modulus (9.3 compared to 8.5) and just over a 16 % increase in characteristic strength making them a more robust option for IT-SOFC applications.
- 6. Analysis of the pore size and pore distribution revealed that the addition of TiO<sub>2</sub> slightly increases the apparent porosity of TDC pellets. Nevertheless, it contributed to a more homogenous pore size distribution with smaller pores, resulting in increased Weibull parameters.
- 7. Close examination of  $CeO_2$  pore geometry and location revealed pores were located along grain boundaries and exhibited a larger radius of curvature compared to the 0.1 wt % TDC pellets. It is presumed that the geometry and larger radius of the pores in  $CeO_2$  samples acted as stress concentrators in the applied stress field, making crack propagation more likely to occur along the weakened grain boundaries (i.e., intergranular fracture). The fracture mode in the 0.1 wt % TDC was primarily transgranular fracture.

#### CRediT authorship contribution statement

Adrianna E. Lupercio: Writing - review & editing, Writing - original draft, Validation, Project administration, Methodology, Investigation, Formal analysis, Data curation, Conceptualization. Riley C. Van Horn: Methodology, Investigation. Cayden Doyle: Methodology, Investigation. Alex Nadermann: Methodology, Investigation. Andrew T. Nelson: Writing – review & editing, Resources, Funding acquisition, Conceptualization. Brian J. Jaques: Writing - review & editing, Supervision, Resources, Project administration, Funding acquisition, Conceptualization.

### Declaration of competing interest

The authors declare that they have no known competing financial interests or personal relationships that could have appeared to influence the work reported in this paper.

#### Acknowledgments

This work was supported in part by the Advanced Fuels Campaign and the Nuclear Energy University Program of the U.S. Department of Energy, Office of Nuclear Energy.

#### References

- [1] T.D. Morrison, E.S. Wood, P.F. Weck, E. Kim, S.O. Woo, A.T. Nelson, D.G. Naugle, A comprehensive assessment of the low-temperature thermal properties and thermodynamic functions of CeO<sub>2</sub>, J. Chem. Phys. 151 (4) (2019).
- M. Kurian, Cerium oxide based materials for water treatment a review J. Environ. Chem. Eng. 8 (5) (2020) 104439.
- [3] E. Park, W. Gallagher, Z. Hobbs, M. Mayton, Pollution prevention via recovery of cerium (IV) oxide in optics company, Case Studies in Chemical and Environmental Engineering 1 (2020) 100003.
- [4] D.E. Tew, R.A. Cox-Galhotra, V.R. Lecoustre, M. Lyubovsky, G.L. Soloveichik, Perspective—the role of solid oxide fuel cells in our carbon-neutral future, J. Electrochem. Soc. 169 (2) (2022) 024508.
- Y.-P. Fu, Y.-C. Liu, S.-H. Hu, Aqueous tape casting and crystallization behavior of gadolinium-doped ceria, Ceram. Int. 35 (8) (2009) 3153-3159.
- [6] M. Zhu, L. Yi, R. Zhou, C. Du, C. Tian, J. Yang, Microstructural, electrical and thermal characterization of  $\mathrm{Dy}^{3+}$ ,  $\mathrm{Sm}^{3+}$ ,  $\mathrm{Er}^{3+}$ ,  $\mathrm{Y}^{3+}$  and  $\mathrm{Gd}^{3+}$  multi-doped cerium dioxide as SOFCs solid electrolytes, J. Alloys Compd. 976 (2024) 173108.
- C. Qiao, J. Yu, S.-q. Hu, X. Ding, W.-t. Yang, S.-y. Li, G.-q. Lv, W.-h. Ma, Microstructure and electrical conductivity of La<sub>10</sub>Si<sub>6</sub>O<sub>27</sub>-La<sub>0.9</sub>Sr<sub>0.1</sub>Ga<sub>0.8</sub>Mg<sub>0.2</sub>O<sub>2.85</sub> composite electrolytes for SOFCs, Ceram. Int. 50 (2) (2024) 3672-3679. Part B.
- X. Sun, S. Deng, Y. Xia, B. Li, Y. Tian, J. Chen, Effect of TiO<sub>2</sub> as an additive on the sintering performance of Sm-doped CeO2-based electrolyte for solid oxide fuel cells, Front. Chem. 10 (2022).
- [9] W. Zając, L. Suescun, K. Świerczek, J. Molenda, Structural and electrical properties of grain boundaries in Ce<sub>0.85</sub>Gd<sub>0.15</sub>O<sub>1.925</sub> solid electrolyte modified by addition of transition metal ions, J. Power Sources 194 (1) (2009) 2-9.
- [10] K.A. González-García, J.A. Díaz-Guillén, S.M. Montemayor, G. Martínez-De la Rosa, O.J. Durá, M.E. Bazaldúa-Medellín, O. Burciaga-Díaz, J.C. Díaz-Guillén, Electrical and thermal properties of LT-SOFC solid electrolytes: Sm cerates/zirconates obtained by mechanochemistry, Int. J. Hydrogen Energy (2024). https://doi. org/10.1016/j.ijhydene.2024.01.057.
- [11] J.X. Zhu, D.F. Zhou, S.R. Guo, J.F. Ye, X.F. Hao, X.Q. Cao, J. Meng, Grain boundary conductivity of high purity neodymium-doped ceria nanosystem with and without the doping of molybdenum oxide, J. Power Sources 174 (1) (2007) 114-123.
- [12] E.Y. Pikalova, V.I. Maragou, A.K. Demin, A.A. Murashkina, P.E. Tsiakaras, Synthesis and electrophysical properties of (1-x)Ce<sub>0.8</sub>Gd<sub>0.2</sub>O<sub>2-8</sub>+xTiO<sub>2</sub> (x=0-0.06) solid-state solutions, Solid State Ionics 179 (27) (2008) 1557-1561.
- [13] P.-L. Chen, I.-W. Chen, Grain growth in CeO<sub>2</sub>; dopant effects, defect mechanism, and solute drag, J. Am. Ceram. Soc. 79 (7) (1996) 1793-1800.
- Y. Sun, C. Wang, Y. Chen, Molecular dynamics simulations of the deformation behavior of gadolinia-doped ceria solid electrolytes under tensile loading, J. Power Sources 233 (2013) 131-138.
- [15] S. Omar, J.C. Nino, Consistency in the chemical expansion of fluorites: a thermal revision of the doped ceria, Acta Mater, 61 (14) (2013) 5406-5413.
- [16] Y.M. Chiang, E.B. Lavik, D.A. Blom, Defect thermodynamics and electrical properties of nanocrystalline oxides: pure and doped CeO2, Nanostruct. Mater. 9 (1) (1997) 633–642.
- [17] K. Suzuki, M. Kato, T. Sunaoshi, H. Uno, U. Carvajal-Nunez, A.T. Nelson, K. J. McClellan, Thermal and mechanical properties of CeO2, J. Am. Ceram. Soc. 102 (4) (2019) 1994-2008.
- [18] A.T. Nelson, D.R. Rittman, J.T. White, J.T. Dunwoody, M. Kato, K.J. McClellan, An evaluation of the thermophysical properties of stoichiometric  $CeO_2$  in comparison to UO2 and PuO2, J. Am. Ceram. Soc. 97 (11) (2014) 3652-3659.

- [19] ASTMC1161-13, Standard Test Method for Flexural Strength of Advanced Ceramics at Ambient Temperature, ASTM International, 2013.
- G. Quinn, L. Ives, S. Jahanmir, Machining cracks in finished ceramics, Key Eng. Mater. 290 (2005) 1-13.
- [21] K.R. McKinney, C.M. Herbert, Effect of surface finish on structural ceramic failure, J. Am. Ceram. Soc. 53 (9) (1970).
- R. Morrell, Biaxial Flexural Strength Testing of Ceramic Materials, National Physical Laboratory, 1998, p. 12.
- [23] A. International, ASTM C1499-15: Standard Test Method for Monotonic Equibiaxial Flexural Strength of Advanced Ceramics at Ambient Temperature, 2019. West Conshohocken, PA.
- [24] G. deWith, H.H.M. Wigemans, Ball-on-ring test revisited, J. Am. Ceram. Soc. 72 (8)
- [25] D.K. Shetty, A.R. Rosenfield, P. McGuire, G.K. Bansal, W.H. Duckworth, Biaxial flexure tests for ceramics, Ceramic Bulletin 59 (12) (1980).
- [26] A.E. Lupercio, E. Moshkelgosha, R.C. Winters, C. Doyle, M. Mamivand, A. T. Nelson, B.J. Jaques, Ball-on-ring test validation for equibiaxial flexural strength testing of engineered ceramics, International Journal of Ceramic Engineering & Science 3 (3) (2021) 128–139.
- [27] A.A. Eliseev, V.A. Efremov, G.M. Kuz'micheva, E.S. Konovalova, V.I. Lazorenko, Y. B. Paderno, S.Y. Khlyustova, X-ray diffraction study of monocrystals of lanthanum, cerium, samarium hexaborides, Kristallografiya 31 (4) (1986) 803-805.
- ASTM E112-12 Standard Test Methods for Determining Average Grain Size, ASTM International, 2013.
- [29] J. Eichler, J. Rodel, U. Eisele, M. Hoffman, Effect of grain size on mechanical properties of submricometer 3Y-TZP: fracture strength and hydrothermal degradation, J. Am. Ceram. Soc. 90 (9) (2007) 2830–2836.
- [30] S. Ban, K.J. Anusavice, Influence of test method on failure stress of brittle dental materials, J. Dent. Res. 69 (12) (1990) 1791-1799.
- [31] S. Poolthong, T. Mori, M. Swain, A comparison of the mechanical properties of three glass-ionemer cements, Dent. Mater. 13 (2) (1994) 220-227.
- [32] A.F. Kirstein, R.M. Wooley, Symmetrical bending of thin circular elastic plates on equally spaced point supports, Journal of Research of the National Bureau of Standards-C. Engineering and Instrumentation 71 (1) (1966).
- A.E. Lupercio, C. Doyle, A.T. Nelson, B.J. Jaques, Equibiaxial flexural strength
- determination of UO<sub>2</sub> using a ball-on-ring test, J. Nucl. Mater. (2023) 154850.

  [34] J.D. McCullough, An X-ray study of the rare-earth oxide systems: Ce<sup>IV</sup>—Nd<sup>III</sup>, Cr<sup>IV</sup>—Pr<sup>III</sup>, Ce<sup>IV</sup>—Pr<sup>IV</sup> and Pr<sup>IV</sup>—Nd<sup>III</sup>, J. Am. Chem. Soc. 72 (3) (1950) 1386–1390.
- [35] R.J. Swope, J.R. Smyth, A.C. Larson, H in rutile-type compounds: I. Single-crystal neutron and X-ray diffraction study of H in rutile, Am. Mineral. 80 (5-6) (1995)
- [36] H.E. Swanson, H.F. McMurdie, M.C. Morris, E.H. Evans, in: N.B.o. Standards (Ed.), Standard X-Ray Diffraction Powder Patterns, United States Department of Commerce, Washington, D.C., 1969, p. 82.
- [37] Q. Zhang, C. Li, High temperature stable anatase phase titanium dioxide films synthesized by mist chemical vapor deposition, Nanomaterials 10 (5) (2020).
- Y. Le Page, M. Marezio, Structural chemistry of magnéli phases  $TinO_{2n-1}$  ( $4 \le n \le n$ 9): IV. Superstructure in Ti<sub>4</sub>O<sub>7</sub> at 140 K, J. Solid State Chem. 53 (1) (1984) 13–21.
- [39] A.K. Lucid, P.R.L. Keating, J.P. Allen, G.W. Watson, Structure and reducibility of CeO2 doped with trivalent cations, J. Phys. Chem. C 120 (41) (2016) 23430-23440.
- [40] D.E. Puente-Martínez, J.A. Díaz-Guillén, S.M. Montemayor, J.C. Díaz-Guillén, O. Burciaga-Díaz, M.E. Bazaldúa-Medellín, M.R. Díaz-Guillén, A.F. Fuentes, High ionic conductivity in CeO<sub>2</sub> SOFC solid electrolytes; effect of Dy doping on their electrical properties, Int. J. Hydrogen Energy 45 (27) (2020) 14062–14070.
- [41] D.E. Puente-Martínez, J.A. Díaz-Guillén, K.A. González-García, S.M. Montemayor, J.C. Díaz-Guillén, O. Burciaga-Díaz, M.E. Bazaldúa-Medellín, K.P. Padmasree Improving the electrical properties of Er-doped CeO2: effect of sintering aids CaO, MgO, and TiO<sub>2</sub> on conductivity, J. Korean Ceram. Soc. 60 (5) (2023) 817–829.
- [42] M.A. Khan, R. Raza, R.B. Lima, M.A. Chaudhry, E. Ahmed, N.R. Khalid, G. Abbas, B. Zhu, N. Nasir, Effect of titania concentration on the grain boundary conductivity of calcium-doped ceria electrolyte, Ceram. Int. 40 (7, Part A) (2014) 9775–9781.
- [43] J.B. Ainscough, F. Rigby, S.C. Osborn, The effect of titania on grain growth and densification of sintered UO2, J. Nucl. Mater. 52 (2) (1974) 191-203.
- W. Weibull, A statistical distribution frunction of wide applicability, J. Appl. Mech. 18 (1951) 293-297.
- [45] K.C. Radford, Effect of fabrication parameters and microstructure on the mechanical strength of UO2 fuel pellets, J. Nucl. Mater. 84 (1979) 222-236.
- [46] M. Lipińska-Chwałek, F. Schulze-Küppers, J. Malzbender, Mechanical properties of pure and doped cerium oxide, J. Eur. Ceram. Soc. 35 (5) (2015) 1539-1547.
- Y. Wang, K.L. Duncan, E.D. Wachsman, F. Ebrahimi, Effects of reduction treatment on fracture properties of cerium oxide, J. Am. Ceram. Soc. 90 (12) (2007) 3908-3914.
- G.J. Pereira, Densification and electrical conductivity of fast fired managanesedoped ceria ceramics, Mater. Lett. 59 (2005) 1195-1199.
- Syed Ismail Ahmad, P. Koteshwar Rao, I.A. Syed, Sintering temperature effect on density, structural and morphological properties of Mg-and Sr-doped ceria, Journal of Taibah University for Science/Science Direct 10 (29 April 2015) 381–385.
- V. Kumar, W.-F. Chen, X. Zhang, Y. Jiang, P. Koshy, C.C. Sorrell, Properties and performance of photocatalytic CeO2, TiO2, and CeO2-TiO2 layered thin films, Ceram. Int. 45 (17, Part A) (2019) 22085-22094.
- [51] H. Matzke, On the effect of  $TiO_2$  additions on sintering of  $UO_2$ , J. Nucl. Mater. 20 (3) (1966) 328–331.

- [52] C.M. Silva, R.D. Hunt, A.T. Nelson, Microstructural and crystallographic effects of sol-gel synthesized Ti-doped UO<sub>2</sub> sintered under reducing conditions, J. Nucl. Mater. 552 (2021) 153003.
- [53] A. Zimmermann, J. Rödel, Generalized orowan-petch plot for brittle fracture, J. Am. Ceram. Soc. 81 (10) (1998) 2527–2532.
- [54] K. Sato, H. Yugami, T. Hashida, Effect of rare-earth oxides on fracture properties of ceria ceramics, J. Mater. Sci. 39 (18) (2004) 5765–5770.
- [55] F.A. Akopov, D.N. Poluboyarinov, Some properties of sintered ceria ceramics, Refractories 6 (3) (1965) 196–201.
- [56] R.A. Cutler, D.L. Meixner, Ceria–lanthanum strontium manganite composites for use in oxygen generation systems, Solid State Ionics 159 (1) (2003) 9–19.
- [57] S.J. Sedler, T.R. Chase, J.H. Davidson, Mechanical properties of gelcast cerium dioxide from 23 to 1500 °c, journal of engineering materials and technology, Transactions of the ASME 139 (1) (2017).
- [58] N. Sammes, G. Tompsett, Y. Zhang, A. Cartner, R. Torrens, The structural and mechanical properties of (CeO<sub>2</sub>)<sub>1-x</sub>(GdO<sub>1.5</sub>)<sub>x</sub> electrolytes, Denki Kagaku Oyobi Kogyo Butsuri Kagaku 64 (6) (1996) 674–680.
- [59] K.R. Reddy, K. Karan, Sinterability, mechanical, microstructural, and electrical properties of gadolinium-doped ceria electrolyte for low-temperature solid oxide fuel cells, J. Electroceram. 15 (1) (2005) 45–56.
- [60] O. Bellon, N.M. Sammes, J. Staniforth, Mechanical properties and electrochemical characterisation of extruded doped cerium oxide for use as an electrolyte for solid oxide fuel cells, J. Power Sources 75 (1) (1998) 116–121.
- [61] K. Yasuda, K. Uemura, T. Shiota, Sintering and mechanical properties of gadolinium-doped ceria ceramics, J. Phys. Conf. 339 (1) (2012) 012006.

- [62] S. Sameshima, T. Ichikawa, M. Kawaminami, Y. Hirata, Thermal and mechanical properties of rare earth-doped ceria ceramics, Mater. Chem. Phys. 61 (1) (1999) 31–35.
- [63] D. Das, M.D.S. Lucio, S. Kultayeva, Y.-W. Kim, Effect of pore size on the flexural strength of porous silicon carbide ceramics, Open Ceramics 17 (2024) 100521.
- [64] R.W. Rice, Ceramic fracture mode-intergranular vs transgranular fracture, PB: 556 pp., in: J.R. Varner, V.D. Frechette, G.D. Quinn (Eds.), Conference: 3. Alfred Conference on Fractography of Glasses and Ceramics, Alfred, NY (United States), 9-12 Jul 1995; Other Information: PBD: 1996; Related Information: Is Part of Ceramic Transactions: Fractography of Glasses and Ceramics III. Volume 64, American Ceramic Society, Westerville, OH (United States), United States, 1996, pp. 1–53. Medium: X; Size
- [65] J.R. Varner, Fracture modes and appearances in ceramics, in: W.T. Becker, R.J. Shipley (Eds.), Failure Analysis and Prevention, ASM International2002, p. 0.
- [66] W. Yan, X. Lin, J. Chen, N. Li, Y. Wei, B. Han, Effect of TiO<sub>2</sub> addition on microstructure and strength of porous spinel (MgAl<sub>2</sub>O<sub>4</sub>) ceramics prepared from magnesite and Al(OH)<sub>3</sub>, J. Alloys Compd. 618 (2015) 287–291.
- [67] V. Gulizzi, C.H. Rycroft, I. Benedetti, Modelling intergranular and transgranular micro-cracking in polycrystalline materials, Comput. Methods Appl. Mech. Eng. 329 (2018) 168–194.
- [68] S. Patnaik, B.W. Spencer, E. Roberts, T.M. Besmann, T.W. Knight, Separate-effects tests for studying temperature-gradient-driven cracking in UO2 pellets, Nucl. Sci. Eng. 195 (12) (2021) 1307–1326.